

Coupling Precipitation Forecasting and Early Warning with Reverse-Martingale Recurrent Neural Networks

Foo Hui-Mean¹ Yuan-chin Ivan Chang^{1,*}

¹Institute of Statistical Science, Academia Sinica, Taipei, Taiwan

*Corresponding author: ycchang@stat.sinica.edu.tw

July 2, 2026

Abstract

Precipitation forecasts are judged by accuracy, but the decisions they support — when to restrict water, when to warn of drought — turn on noticing when a local regime is becoming abnormal, which forecast scores alone do not reveal. We ask whether one recurrent model can do both with little or no loss in forecast skill. We add a backward-coherence (reverse-martingale) penalty that keeps the network’s hidden state smooth when read backward in time; the size of the resulting reconstruction defect becomes an online warning signal, monitored by a sequential change-point detector. The design is deliberately conservative. On real daily station data from four contrasting climates — monsoonal Taiwan, semi-arid Texas, temperate Germany, and Mediterranean Anatolia (Turkey) — the model matches a standard network’s forecast skill everywhere, and makes the hidden state markedly steadier in every region. The novelty is the added information: on these real droughts the signal can alarm well ahead of the operational SPI-3 index, giving lead that neither the forecast nor the index provides. This benefit is not uniform across the four regions — large in one, partial in two others, and near-absent in the fourth. We offer the hydroclimatic character of drought onset, whether it precedes or merely coincides with the rainfall deficit, as a plausible explanation to be tested in future work, supported by a controlled synthetic study with known onset times. The contribution is thus a new and conservative way to read precipitation records: no loss in forecast skill, a steadier model, and an early-warning signal beyond the standard index.

Keywords: precipitation nowcasting; probabilistic forecast verification; drought early warning; sequential change-point detection; hidden-state monitoring; recurrent neural networks; Taiwan; Texas; Germany; Turkey; GHCN-Daily.

Highlights

- A backward-coherence penalty turns a precipitation RNN into a warning sensor
- Forecast skill is preserved across four contrasting real climate regions

- The hidden-state defect can alarm drought onset ahead of the SPI-3 index
- Lead is region-dependent: largest where onset precedes the rainfall deficit
- A synthetic study with known onset times explains where the advantage holds

1 Introduction

Operational hydrometeorology increasingly needs precipitation products that serve not only as forecasts but also as warnings. Reservoir operations, irrigation, urban drainage, drought mitigation, and flash-flood response all depend on detecting damaging regimes early enough for action [8, 20]. This is especially difficult at small spatial scales, where local precipitation is shaped by terrain, land–sea contrast, convective organization, and rapidly evolving moisture transport [15]. As a result, a model may achieve reasonable average forecast scores while still issuing warnings that are late, noisy, or poorly calibrated.

Deep recurrent models, including LSTM [7], GRU [6], ConvLSTM [21], and Pre-dRNN [23], are well suited to extracting temporal structure from gauge, satellite, radar, and reanalysis sequences. For operational warning, however, the forecast value alone is often insufficient. Thresholding a predicted rain rate, accumulated precipitation total, or drought index treats warning as post-processing and ignores information in the evolving hidden state. This separation is especially limiting when drought, monsoon transition, typhoon rainbands, or flash-flood-producing regimes begin to emerge before local precipitation thresholds are crossed [10, 14].

Operational drought monitoring and prediction is itself a mature field, spanning multi-source indicators, statistical and dynamical prediction, uncertainty communication, and user-oriented early warning at regional to global scales [11]. Within that broad agenda we pursue a narrower, complementary question: given a recurrent precipitation forecasting model, how can its evolving internal state be used to produce a stable, calibrated drought-warning signal? To that end, this paper develops a forecast-preserving warning framework for local, station-scale precipitation. The key idea is to regularize the recurrent hidden state so that ordinary hydroclimatic evolution remains coherent when read backward through a learned one-step projector. The resulting backward-coherence residual is computed online and passed to a sequential change-point detector, allowing the same hidden trajectory to produce both the precipitation forecast and a calibrated drought–flood warning signal. The aim is deliberately conservative: rather than improving ordinary forecast accuracy, the method seeks to add early-warning capability with little or no loss in forecast skill. We therefore ask whether reverse-martingale (RM) regularization can preserve GRU-level forecast performance while turning the hidden-state trajectory into a useful warning diagnostic, and in which hydroclimatic settings it provides meaningful lead time.

Main contributions. This paper introduces a forecast-preserving warning workflow for local precipitation. A recurrent model produces the usual probabilistic forecast while its hidden-state trajectory also yields an online RM defect, $d_t = \|h_{t-1} - g_\phi(h_t)\|$, computed after the observation at time t is assimilated. The standardized defect drives a one-sided CUSUM detector calibrated by ARL_0 on held-out climatology. We evaluate the framework on four real daily station networks representing distinct precipitation climates: monsoonal, mountainous Taiwan; semi-arid Texas Hill Country; temperate, maritime-influenced Germany; and Mediterranean-continental Turkey (Section 3). Across all four

regions, the reverse-martingale recurrent neural network (RMRNN) preserves GRU-level forecast and heavy-rain warning skill while reducing hidden-state path instability by 43–55% in Q_{path} . The novelty is in what the same model *additionally* provides: an early-warning signal, read directly from the hidden state, that on these real droughts can alarm well ahead of the operational SPI-3 index — information that neither the forecast nor the standard index supplies. This added lead is not uniform across the four regions — large in semi-arid Texas, smaller but still positive in temperate Germany, marginal in Mediterranean-continental Turkey, and near zero in monsoonal Taiwan. We do *not* treat this variation as an established effect of landform: establishing that would require many more regions and is beyond the scope of this paper. We instead report it as an observation and offer the hydroclimatic character of drought onset — whether it precedes or merely coincides with the rainfall deficit — as a plausible explanation to be tested in future work. A controlled synthetic study with known injected onsets supports this reading: the defect leads for slow-onset drought but not for sharp heavy-rain onset, which is already visible in precipitation itself (Section 4.3).

The rest of the paper is organized as follows. Section 2 presents the coupled forecasting-and-warning workflow, with RM details deferred to Appendix A. Section 3 gives the real-data evaluation. Section 4 presents the controlled synthetic experiments, including false-alarm calibration and the multi-variable defect. Sections 5 and 6 discuss implications, limitations, and operational extensions. Additional synthetic results and full data-acquisition and preprocessing details are provided in the online supplement.

2 Forecasting and Warning Workflow

This section presents the operational version of the proposed method. The central idea is simple: the recurrent model produces a standard precipitation forecast, while its hidden-state trajectory is monitored for unusual departures from normal local evolution. The main text focuses on the forecasting-and-warning workflow; formal reverse-martingale notation, loss functions, and implementation details are collected in Appendix A.

2.1 Local inputs and forecast target

At each issue time, the model uses recent meteorological observations from a small neighborhood around the target basin, station, or grid cell. Inputs vary by dataset and may include precipitation, temperature, humidity, vorticity, soil moisture, and low-level winds. Neighborhood radius is tuned for the Taiwan CWA network, where precipitation is strongly shaped by orographic and basin-scale effects, and fixed for the lower-density CHIRPS and GHCN-Daily applications. Full notation is provided in Appendix A.

The recurrent model encodes local meteorological history into a hidden state h_t and produces a probabilistic accumulated-precipitation forecast at the chosen lead time. To handle frequent zeros and a skewed positive tail, precipitation is modeled with a mixed distribution: a dry probability for zero rainfall and a log-normal distribution for positive amounts, following Sloughter et al. [22]. We use the Continuous Ranked Probability Score CRPS as the primary verification metric and report RMSE and MAE for comparison.

2.2 Backward coherence as a warning diagnostic

The reverse-martingale regularizer encourages neighboring hidden states to remain coherent during typical hydroclimatic evolution. It promotes hidden trajectories in which each subsequent state retains enough information to approximately reconstruct the previous state. Smooth local weather evolution should therefore yield small reconstruction defects, while abrupt transitions—such as drought onsets, monsoon shifts, frontal passages, or typhoon rainbands—should produce larger, measurable departures.

A key directionality applies to drought: once a sustained dry regime sets in, precipitation variability drops and atmospheric dynamics become simpler and more repetitive. The hidden state therefore evolves more predictably, and the backward projector g_ϕ reconstructs it more accurately — so the defect d_t *decreases* relative to its climatological level. The CUSUM monitors this *downward* shift as a drought signal (Section 2.3). The opposite applies to the onset of heavy-rain events, which raises the defect.

This regularizer does not assume that precipitation follows a martingale, nor is it designed to minimize RMSE. Its purpose is to make the hidden state useful as a stability diagnostic while preserving forecast skill. The joint objective combines the standard precipitation loss with a backward-coherence penalty; the loss function, training schedule, and projector architecture are detailed in Appendix A.

2.3 Online residual and alarm rule

For operational use, the warning residual must be available when an alert is issued. After assimilating the observation at valid time t and updating the hidden state, we compute

$$d_t = \|h_{t-1} - g_\phi(h_t)\|, \quad (1)$$

where g_ϕ is the learned backward projector. Because this defect uses only information available up to time t , we set $r_t \equiv d_t$ in the warning experiments.

We standardize the residual on pre-event climatology and monitor it with a one-sided cumulative-sum (CUSUM) sequential change-point detector [18],

$$S_t = \max(0, S_{t-1} + z_t - k), \quad S_0 = 0, \quad (2)$$

with reference value $k = 1/2$, where z_t is the standardized defect. The sign of z_t is chosen to match the expected direction of the regime shift: for *drought*, the defect decreases under a dry regime (as explained in Section 2), so we monitor a downward shift (i.e. negate z_t before accumulating); for *heavy-rain onset*, the defect increases, so we monitor an upward shift directly. This means the CUSUM statistic S_t always increases under the regime of concern, regardless of direction. The detector alarms when S_t first exceeds a threshold h calibrated to a target no-change average run length, ARL_0 , by Monte Carlo simulation on held-out climatological periods rather than by asymptotic formulas alone. We use the additive CUSUM because the standardized reverse-martingale defect is strongly right-skewed and autocorrelated: it is the classical sequential detector for exactly this heavy-tailed, dependent setting, and it attains the target ARL_0 stably where a multiplicative recursion would be driven to premature alarms by occasional large values. All warning results in Section 4.3 use this detector.

Algorithm 1. *Residual-driven sequential warning detector (the one-sided CUSUM of Eq. (2), Section 2.3).*

Require: Trained recurrent model and backward projector; held-out no-change climatology; target ARL_0 ; reference value $k = 1/2$; shift direction for the regime ($-$ for drought, $+$ for heavy-rain onset).

Ensure: Calibrated threshold and online alarm sequence.

1. Compute online hidden-state residuals $r_t = \|h_{t-1} - g_\phi(h_t)\|$ on the held-out null climatology.
2. Estimate the null location $\hat{\mu}_0$ and scale $\hat{\sigma}_0$ (after the variance-stabilizing transform described in Appendix A) and form the standardized residual $z_t = (r_t - \hat{\mu}_0)/\hat{\sigma}_0$.
3. Run the one-sided CUSUM $S_t = \max(0, S_{t-1} + s z_t - k)$ where s is the regime shift direction, and select the threshold h via Monte Carlo sampling on bootstrapped null segments such that the mean time to a false alarm matches the target ARL_0 .
4. During online operation, update the hidden state h_t upon receiving each new observation, compute r_t and z_t , update S_t , and trigger an alarm at the first instance where $S_t \geq h$.

3 Real-Data Evaluation

We begin with real observations across multiple landforms, since the paper’s operational claims concern real precipitation. The four networks are chosen to be *deliberately contrasting along two axes at once*: four distinct landform-and-weather regimes — monsoonal and steeply orographic, semi-arid subtropical, temperate maritime, and Mediterranean-continental — sampled at four widely separated locations on the globe (East Asia, North America, Central Europe, and the eastern Mediterranean). Spanning both climate type and geographic setting is deliberate: a property that holds across all four is unlikely to be an artefact of any single region’s climate, terrain, observing network, or particular drought, so the comparison is a genuine generalization test rather than a single-region demonstration — and, as it turns out, the contrast also surfaces a regime-dependence in the warning lead that a single-region study would have hidden. We evaluate the *Taiwan CWA* archive, with monsoonal rainfall, typhoons, and steep orography; the *Texas Hill Country* GHCN-Daily network, a semi-arid subtropical region prone to drought and flash floods; the *Germany* GHCN-Daily network, a temperate, maritime-influenced region affected by the 2018 Central-European drought; and the *Turkey* GHCN-Daily network, a Mediterranean-continental Anatolian region affected by the 2013–2014 Turkish drought. Each network is processed identically and treated as a set of single-station replications. Data sources, quality control, and preprocessing are documented in the online supplement, Section ???. Two findings hold in every region, while a third is region-dependent. We discuss these results in turn before presenting a controlled synthetic study in Section 4, where known onset times allow us to corroborate and explain the real-data findings.

3.1 Data, preprocessing, and evaluation metrics

Data and preprocessing (summary). The Taiwan series come from the CWA/CODiS historical archive (the registration-free *Raingel/historical_weather* reconstruction); the Texas Hill Country, Germany, and Turkey series from the NOAA GHCN-Daily archive [17], with stations selected by bounding box and adequate daily-precipitation coverage. Full URLs and retrieval scripts are given in the data-availability statement. For each region we use a strict chronological split — an early segment for training, a later disjoint segment for null calibration of the detector, and a final segment for evaluation, with any declared drought-event years excluded from calibration. Short gaps are linearly interpolated, remaining missing days set to 0 mm, and values $\log(1+x)$ -transformed and standardised per station on the training split; stations with more than 25% missing days are dropped. For the warning study each monitored stream is additionally deseasonalised by its pre-event day-of-year climatology, and the SPI-3 proxy is a 90-day running accumulation. Every detector is calibrated to a common no-change average run length ARL_0 of one year by Monte-Carlo bootstrap on the null window. The per-region station lists, exact windows, and the literal commands are in the online supplement (Section ??).

Evaluation metrics. *Test MSE/MAE* are next-day errors on standardised log-precipitation. $Q_{\text{path}} = \sum_t \|h_{t+1} - h_t\|$ is the total hidden-state path increment, a model-agnostic measure of trajectory instability (smaller is more stable). Intuitively, Q_{path} measures the total “distance travelled” by the hidden state across all time steps: a model whose internal representation changes smoothly from day to day gives a small Q_{path} , whereas one that jumps erratically gives a large value. Because Q_{path} depends only on the hidden states themselves, it can be computed and compared for *any* recurrent model, including those without an RM penalty. It is related to but distinct from the squared backward-projector defect $\hat{Q} = \sum_t \|h_t - g_\phi(h_{t+1})\|^2$ used in the appendix, which additionally requires the learned reverse map g_ϕ and is used during training; Q_{path} is used here as an architecture-neutral stability diagnostic. *AUC(P95)* and *CSI* score next-day exceedance of each station’s local 95th-percentile daily total (ROC area, and a base-rate-calibrated critical success index). For the sequential warning, the *detection rate* is the fraction of events alarmed within the post-onset horizon, and the *paired lead* is

$$\text{Lead} = \text{alarm}(\text{SPI-3}) - \text{alarm}(\text{RM}), \quad (3)$$

positive when the RM alarm is earlier. Results are summarised as medians over ten random seeds, per station.

Model and training configuration. Table 1 summarises the model and training settings, which are shared across all regions and experiments unless noted; full details and the reverse-martingale loss are in Appendix A.

3.2 Forecast skill and path stability across landforms

For each network, we compare next-day forecast error, hidden-state path instability Q_{path} , and heavy-rain warning skill for RMRNN, its unregularized ablation $\text{RMRNN}_{\lambda=0}$ (the identical architecture with the RM penalty switched off), and a GRU; see Table 2. The pattern is consistent across all four climates. RMRNN matches GRU and the $\text{RM-RNN}_{\lambda=0}$ ablation in forecast accuracy within $\pm 0.5\%$ in test MSE while roughly halving

Table 1: Model and training configuration, shared across regions.

Setting	Value
Recurrent cell (RMRNN, $\lambda=0$ ablation)	Elman, full BPTT
Learned baselines	GRU, LSTM, causal TCN
Non-learned baselines	persistence, climatology, SPI-3, raw deficit
Hidden dimension	32
Input window	30 days (1–6 h for hourly products)
Optimizer / learning rate	Adam / 5×10^{-3}
Epochs / warm-up	200 / 5
RM penalty schedule λ	0.1 \rightarrow 0.01 (post-warm-up decay)
Forecast/stability seeds	1 per station
Warning-study seeds	10 per station
Hyperparameters across regions	shared (fixed by validation)

hidden-state path instability, reducing Q_{path} by 43–55% relative to the unregularized network. Heavy-rain next-day warning skill, measured by AUC, is also preserved, with RMRNN and GRU indistinguishable within noise in every region. These are the two universal real-data findings: reverse-martingale regularization stabilizes the recurrent trajectory without measurable loss in forecast accuracy or heavy-rain warning skill across four independent observational networks.

Table 2: Forecast skill and hidden-state path stability on four real station networks. Each row block is one network (n stations used after quality control); values are mean \pm SD across stations. Q_{path} is the hidden-state path-instability diagnostic (lower is more stable). RMRNN preserves GRU-level MSE/MAE/AUC while sharply reducing Q_{path} .

Region (n)	Model	Test MSE	Test MAE	Q_{path}	AUC(P95)
Texas (39)	RMRNN	0.816 \pm 0.135	0.556 \pm 0.070	4.90 \pm 1.23	0.691 \pm 0.054
	RMRNN $_{\lambda=0}$	0.814 \pm 0.134	0.558 \pm 0.052	9.70 \pm 2.53	0.682 \pm 0.046
	GRU	0.814 \pm 0.134	0.548 \pm 0.058	7.13 \pm 1.76	0.704 \pm 0.049
Germany (49)	RMRNN	0.875 \pm 0.130	0.737 \pm 0.054	7.54 \pm 1.63	0.674 \pm 0.052
	RMRNN $_{\lambda=0}$	0.873 \pm 0.132	0.730 \pm 0.055	14.29 \pm 3.03	0.672 \pm 0.051
	GRU	0.867 \pm 0.144	0.727 \pm 0.070	10.87 \pm 2.34	0.674 \pm 0.051
Turkey (24)	RMRNN	0.832 \pm 0.140	0.624 \pm 0.070	6.94 \pm 1.44	0.781 \pm 0.046
	RMRNN $_{\lambda=0}$	0.826 \pm 0.136	0.620 \pm 0.066	15.31 \pm 3.44	0.770 \pm 0.041
	GRU	0.818 \pm 0.139	0.601 \pm 0.070	10.60 \pm 2.51	0.790 \pm 0.040
Taiwan (21)	RMRNN	0.777 \pm 0.079	0.642 \pm 0.068	8.73 \pm 1.60	0.803 \pm 0.044
	RMRNN $_{\lambda=0}$	0.780 \pm 0.067	0.639 \pm 0.068	15.41 \pm 2.92	0.801 \pm 0.046
	GRU	0.769 \pm 0.072	0.637 \pm 0.073	11.07 \pm 1.79	0.805 \pm 0.045

3.3 A drought-warning signal beyond the standard index, and its variation across regions

The hidden-state defect supplies a quantity that a forecast and an accumulation index do not: an online estimate of how far the local regime has departed from its trained

climatology. We ask what this added signal is worth as a drought warning by applying the detector to one documented multi-year drought in each region — Texas 2010–2015, Germany 2018–2019, Turkey 2013–2014, and Taiwan 2020–2021 — and comparing the lead of the RM-defect CUSUM against an SPI-3 CUSUM at matched ARL_0 (Table 3, Figure 1). Unlike the uniform forecast-preservation result above, the warning lead differs across the four regions. We present the regions in order of decreasing lead. The lead appears to track how much of the drought-onset signal is already carried by the accumulated precipitation deficit that SPI-3 measures: largest in aperiodic semi-arid flash drought (Texas), positive but smaller in temperate Germany, marginal in Mediterranean-continental Turkey, and near zero in monsoonal Taiwan, where the rainfall deficit and the onset largely coincide. We stress that this is an interpretation of four cases, not a demonstrated law; with only four regions and one event each we cannot establish landform or hydroclimate as a quantitative factor, and we return to this as a direction for future work (Section 5). In semi-arid *Texas*, the RM-defect alarm leads SPI-3 by a median of about +140 days, or roughly 4.5 months, with consistent region-wide gains: RM is earlier in 92% of runs, and 34/39 stations have a positive median lead. In temperate *Germany* (the 2018 Central-European drought) the lead is positive but more modest — a median of about +50 days, RM earlier in 74% of runs and at 34/49 stations. In Mediterranean-continental *Turkey* (the 2013–2014 Anatolian drought) the lead is positive but marginal and strongly station-dependent: the pooled median is about +13 days, RM is earlier in 54% of runs, and 12/24 stations have a positive median lead. In monsoonal *Taiwan*, the advantage is regional rather than island-wide: the defect leads in central mountain water-supply catchments but lags on the wet windward coast, leaving the pooled median lead near zero (−17 days, RM earlier in 48% of runs). Section 3.4 analyzes this orographic split.

Table 3: Drought-warning lead of the RM-defect CUSUM over the SPI-3 CUSUM at matched ARL_0 of one false alarm per year. Detection columns give mean per-station detection rates. Lead is in days, with positive values indicating earlier RM alarms. Median lead is the pooled station \times seed median; mean lead is reported with standard deviation to show within-region spread. RM leads strongly in Texas, moderately in Germany, marginally in Turkey, and is near neutral in Taiwan.

Region	n	RM det.	SPI det.	Median lead (d)	Mean lead (d)	RM earlier
Texas	39	96%	92%	+140	+136 \pm 121	92%
Germany	49	89%	94%	+50	+64 \pm 287	74%
Turkey	24	95%	92%	+13	-92 \pm 315	54%
Taiwan	22	83%	77%	-17	-49 \pm 156	48%

The mechanism is consistent across the four cases: the RM defect leads SPI-3 exactly when drought onset is a *regime shift in the multivariate dynamics* that precedes the accumulated precipitation deficit (semi-arid flash-drought, and the orographically sheltered Taiwan catchments), and shrinks toward zero when the rainfall deficit and the onset largely coincide (monsoonal Taiwan, and the seasonal Anatolian drought). The method’s early-warning value is therefore conditional on hydroclimate, a point we return to in Section 5. The remainder of this section dissects the Taiwan case, whose within-region orographic split is the clearest illustration of this mechanism on real data.

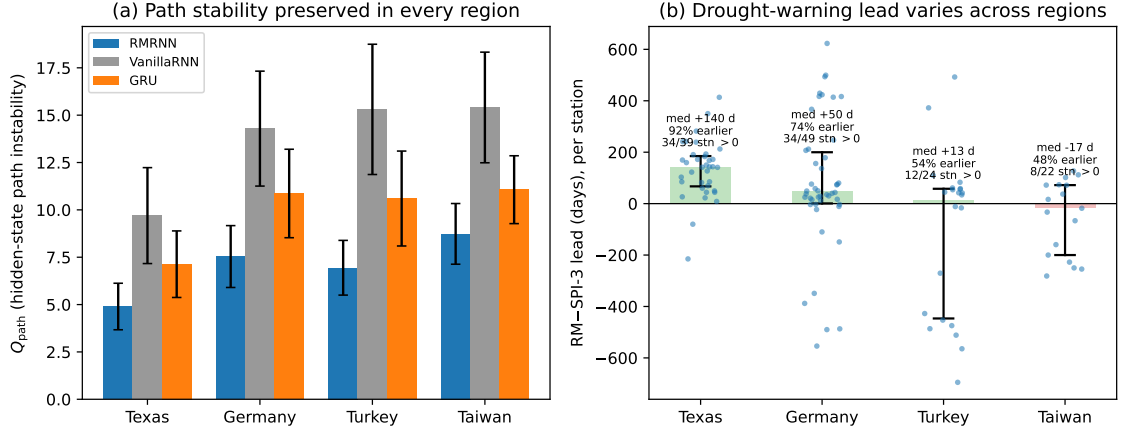


Figure 1: **Real data, four regions.** (a) Hidden-state path instability Q_{path} is reduced by RMRNN relative to the unregularized network in every region (bars are means, error bars ± 1 SD across stations; forecast skill preserved, Table 2). (b) The drought-warning lead of the RM-defect over SPI-3 varies across the four regions: strongly positive in semi-arid Texas, moderate in temperate Germany, marginal in Mediterranean-continental Turkey, and near zero in monsoonal Taiwan. Shaded bars are the pooled median lead; points are per-station median leads and the vertical whisker is their inter-station interquartile range, so the substantial within-region spread (and the fraction of stations with a positive lead) is shown explicitly rather than hidden behind the point estimate.

3.4 Regional structure of the lead: the 2020–2021 Taiwan drought

Real CWA station data and setup. Both real Taiwan evaluations use the open *Taiwan Historical Meteorological Observations* archive (Raingel/historical_weather), a registration-free reconstruction of the CWA CODiS database. The forecast/path-stability ablation (Section 3.2) uses 23 synoptic stations over 1998–2020, 21 after a missingness filter (Appendix A.6). For the present event study we draw a separate, deliberately broad island-wide set of 22 quality-filtered stations spanning 2012–2022 — broad because restricting to the drought core would bias the island-wide picture, as shown below.

We examine the Taiwan case behind the near-zero pooled lead in Table 3 because its within-region structure is the clearest single-region illustration of the mechanism. The 2020–2021 drought was Taiwan’s worst in 56 years: the 2020 typhoon season made no landfall (a first in roughly six decades) and June 2020–May 2021 rainfall ran about one third of normal, drawing several reservoirs below 5% capacity. For each station an RMRNN is trained on 2012–2016, every detector is calibrated to a common one-year ARL_0 on a 2017–2019 null window, and a CUSUM on the RM defect and a CUSUM on a 90-day SPI-3 accumulation proxy are run over 2020-01–2021-08, monitoring a downward shift. Both streams are deseasonalised by their pre-2020 day-of-year climatology (Appendix A.6); without this neither fires, the drought anomaly being smaller than the seasonal swing. The lead is the paired difference $\text{alarm}(\text{SPI-3}) - \text{alarm}(\text{RM})$ (positive = RM earlier), reported as per-station medians over ten seeds.

The result is fundamentally a *terrain-dependent effect*. Taiwan’s high central mountains and narrow coastal plains create sharply different precipitation regimes within a 400×150 km island, so a single island-wide average would mix physically distinct responses. We therefore map the per-station lead directly onto the island; see Figure 2, Table 4, and Appendix A.8. We interpret the results by terrain rather than collapsing

them to one number.

The map shows a coherent, physically interpretable pattern. The RM-defect detector leads — by two to four months — over the *central mountain water-supply catchments*: Taichung (+127 d), Sun Moon Lake (+112 d), Yushan (+102 d), Wuqi (+74 d) and Alishan (+72 d) — positive at all five of these listed headwater stations — the high-elevation sources of the reservoirs that fell below 5% capacity, where the RM alarm clusters in April–May 2020 well ahead of the accumulation baseline. It *lags* on the wetter *eastern and southeastern coast* (Suao –250 d, Yilan –228 d, Taitung –200 d, Hengchun –255 d), where the northeasterly monsoon kept conditions wet, the meteorological drought was weak or absent, and the precipitation-index early crossings reflect a different regime rather than a missed drought. In the *southwestern lowlands* (Tainan, Kaohsiung, Yongkang) the SPI-3 CUSUM never crosses its matched threshold (Det. SPI = 0), its drought signal swamped by high climatological variance, whereas the RM detector still fires on 40–60% of seeds, recovering a signal the accumulation baseline misses entirely. The lowland station Chiayi, although administratively “central”, behaves like the coast (–282 d), confirming that the controlling variable is orography — mountain headwater versus lowland/coast — not compass region.

This terrain-dependent effect has a natural explanation. Taiwan’s Central Mountain Range rises from sea level to nearly 4,000 m over a few tens of kilometres and is among the steepest, most rapidly eroding landscapes on Earth, drained by short, steep rivers with little channel or subsurface storage [2, 3]. In such catchments a precipitation deficit is poorly buffered: once the sustaining orographic rainfall shuts off, the catchment dries quickly and the meteorological deficit becomes a hydrological one with little delay. Consistent with this, hydrological drought in Taiwan responds faster to rainfall deficits than agricultural drought, with the central and southern uplands the principal drought hotspots [4]. The regime the defect monitors therefore turns sharply and early in exactly these steep headwater catchments that feed the reservoirs, whereas on the wetter eastern and southeastern coasts the winter monsoon sustains windward orographic rainfall [1] and lowland storage buffers short deficits, leaving no comparably crisp transition to detect ahead of the slow accumulation index. The lead thus appears where steep terrain and poor water retention make drought both fastest to develop and most consequential.

We therefore report the drought result *by terrain* rather than as an island aggregate; the formal island-wide average is, as expected, not significant (median –18 d over 17 paired stations; bootstrap 95% CI [–200, +72] d), which is precisely why averaging is the wrong lens. The controlled synthetic study (Section 4.3) isolates a *single* homogeneous regime with a known onset, where the lead is uniform; that idealized case is the behaviour of one regime in isolation, which these spatially structured observations reproduce in the mountains but not on the monsoon coasts. The within-Taiwan split is the same mechanism that orders the four regions: a positive lead arises where drought onset is a multivariate regime shift that precedes the accumulated rainfall deficit (the steep mountain headwater catchments here; semi-arid Texas and temperate Germany across regions), and it shrinks toward zero where the rainfall deficit *is* the onset signal (the monsoon coast here; the seasonal Anatolian drought in Turkey). The station-level table is thus a single-island microcosm of the cross-region gradient, with terrain and elevation measured directly rather than inferred.

The wet counterpart: Mei-yu onset. A natural question is whether the same lead appears for the onset of the East-Asian *Mei-yu* (plum-rain) season — the spring-to-

Table 4: Real 2020–2021 Taiwan drought: early-warning lead of the RM-defect CUSUM over the SPI-3 CUSUM at matched ARL_0 , by region, over 22 stations and ten seeds. “Det.” is the mean fraction of seeds on which each detector fires; the median lead = $\text{alarm}(\text{SPI-3}) - \text{alarm}(\text{RM})$ in days (positive = RM earlier) is taken over the region’s stations with a defined paired lead, and “RM earlier” counts those stations. The full per-station breakdown is in Appendix A.8.

Region	#stns	Det. RM	Det. SPI	Median lead (d)	RM earlier
Central water-supply	5	98%	100%	+102	5/5
Northern	5	90%	80%	+10	2/4
Eastern/SE coast	7	77%	100%	−200	1/7
Southern lowland	5	68%	20%	—	0/1
Island-wide	22	83%	77%	−18 (n.s.)	8/17

summer regime transition into sustained frontal rain over Taiwan. We deliberately do not use typhoons here: typhoon rainfall is directly observed and carries no warning lead by construction. Mei-yu onset, by contrast, is a genuine regime change, the wet analogue of drought onset, so a lead is at least physically possible. We repeat the detection protocol for the six Mei-yu seasons of 2017–2022 (12 stations, ten seeds; each year’s onset is one event), calibrating both detectors each year on that year’s pre-Mei-yu spring (March–April) and monitoring 1 May–15 July; the operational baseline is a CUSUM on a 15-day precipitation accumulation. Across all 690 station–year–seed cases both detectors fire almost always (RM 96%, accumulation 99%), but the RM-defect detector provides *no* lead: the median paired lead is -2 days (mean -6 ± 15 d), essentially a tie with the accumulation index and stable across years (per-year medians 0 to -4 d) and stations (positive at only one of twelve). The contrast with the drought result is the central point. The defect leads precisely when the operational index is intrinsically slow — a multi-month accumulating *deficit*, as in drought — and not when the regime change expresses itself in rapidly accumulating rainfall, as at Mei-yu onset, where a short accumulation window already reacts promptly. The real-data advantage is thus specific to slow-onset deficit regimes rather than to wet-versus-dry per se, exactly the boundary the mechanism predicts — and the same boundary that the controlled heavy-rain experiment isolates under a known onset (Section 4.3.3).

3.5 Taiwan ablation detail: per-station stability and deep baselines

We close with a closer look at the Taiwan network, which lets us add an explicit ablation and deep-learning baselines behind the headline Taiwan row of Table 2. Each of the 21 quality-controlled stations is an independent univariate task (a 30-day window of standardised log-precipitation predicting the next day, chronological 80/20 split), and the stations act as natural replications. We compare the Elman RMRNN against the *identical* architecture with $\lambda = 0$, so any difference is attributable to the RM penalty alone, and report next-day MSE and MAE, the model-agnostic hidden-path increment $Q_{\text{path}} = \sum_t \|h_{t+1} - h_t\|$, and heavy-rain early-warning skill (next-day exceedance of each station’s 95th percentile; ROC AUC and CSI).

Table 5 summarises the comparison. RM regularization reduces Q_{path} by 43% (8.7

vs. 15.4) at *every one* of the 21 stations (mean -42.9%), while next-day MSE, MAE, AUC, and CSI are all statistically indistinguishable from the $\lambda = 0$ arm. The same holds against a GRU trained by the identical protocol: it matches on skill, but its hidden-path instability (11.1) sits between the unregularized network (15.4) and RMRNN (8.7) — gating buys some stability, explicit RM regularization buys more, at no cost to skill. Two off-the-shelf deep baselines, a single-layer LSTM and a causal temporal convolutional network (TCN), are statistically tied with RMRNN and the GRU on every skill metric, yet RMRNN retains the *lowest* Q_{path} of all, below even the LSTM’s 9.5; that the non-recurrent TCN also matches on skill confirms that the one-step task does not require a carefully shaped recurrent state — which is precisely why the contribution is the *stabilised hidden state and the warning residual it supports*, not raw forecast skill, on which all five models are interchangeable here.

Table 5: Real-data forecast-skill and path-stability comparison on the Taiwan CWA historical daily archive (Section 3.4): RMRNN ($\lambda: 0.1 \rightarrow 0.01$), its unregularized ablation RMRNN $_{\lambda=0}$, a standard GRU, and two off-the-shelf deep sequence baselines — an LSTM and a causal dilated temporal convolutional network (TCN) — all trained by the same protocol; mean \pm SD over 21 quality-controlled stations (1998–2020, next-day forecast). $Q_{\text{path}} = \sum_t \|h_{t+1} - h_t\|$ is the hidden-path increment total (undefined for the non-recurrent TCN, marked “—”). Forecast MSE/MAE are on standardised log-precipitation; AUC and CSI are for next-day exceedance of the local 95th percentile. Lower is better for MSE, MAE, Q_{path} ; higher is better for AUC, CSI. Best in each column in **bold**; the skill columns (MSE, MAE, AUC, CSI) are statistically indistinguishable across all five models (overlapping \pm SD bands), whereas Q_{path} separates them.

Model	MSE	MAE	Q_{path}	AUC	CSI
GRU	0.769 \pm 0.072	0.637 \pm 0.073	11.07 \pm 1.79	0.805 \pm 0.045	0.197 \pm 0.059
LSTM	0.767 \pm 0.069	0.634 \pm 0.074	9.51 \pm 1.67	0.805 \pm 0.047	0.199 \pm 0.058
TCN	0.788 \pm 0.070	0.658 \pm 0.069	—	0.798 \pm 0.044	0.192 \pm 0.055
RMRNN $_{\lambda=0}$	0.780 \pm 0.067	0.639 \pm 0.068	15.41 \pm 2.92	0.801 \pm 0.046	0.199 \pm 0.053
RMRNN	0.777 \pm 0.079	0.642 \pm 0.068	8.73 \pm 1.60	0.803 \pm 0.044	0.193 \pm 0.052

The full per-station breakdown behind these averages is reported in Appendix A.7 (Table 10), which shows that the Q_{path} reduction holds at all 21 stations individually. The exact run parameters are produced by `run_taiwan_precip.py` (input window 30 d, hidden dimension 32, Adam learning rate 5×10^{-3} , 200 epochs, seed 42), archived with the paper; the same script writes the per-station path-stability figure.

4 Synthetic Controlled Study

The real-data evaluation of Section 3 established the two universal claims, and showed that the warning lead varies across regions, but real events leave three questions unanswerable on observations alone. First, a real drought has no sharp, known onset, so detection rate, lead, and false-alarm rate cannot be measured against a ground truth — the real leads above are *paired* differences against SPI-3, not against a true onset time. Second, the heavy-rain boundary can be probed only obliquely, because operational heavy-rain warning is next-day exceedance rather than the onset of a sustained wet regime. Third,

the real station networks are precipitation-only, so the multivariate behaviour of the defect cannot be exercised. This section is built to answer exactly these three questions, with a controlled synthetic study that trades realism for the ground truth that makes detection measurable. In other words, the synthetic study is not where the case is made — the real data already made it — but where it is *explained*: it injects a known onset to confirm that the defect detects slow-onset drought and not sharp heavy-rain onset, checks the detector’s false-alarm calibration directly, and exercises the multi-variable defect, so the landform pattern seen on real data becomes a tested mechanism rather than an observed coincidence.

Every quantitative result in this section is therefore obtained on *synthetic* precipitation from domain-calibrated stochastic simulators, not on the raw observational archives. Each simulator is a *controlled twin* of one of the real warning environments — it reproduces that environment’s statistical structure (wet-day frequency, seasonal cycle, gamma-distributed intensity, inter-site correlation, and, for the multi-variable case, the cross-channel covariance of precipitation with temperature, soil moisture, and wind) — but, unlike the real records, a regime change (drought or heavy-rain onset) is injected at a *known* time. This lets us measure detection rate, lead, and false-alarm rate against a ground-truth onset that no single historical event can provide. A sub-daily flash-flood study remains the principal outstanding extension (Section 5).

4.1 Target environments for the simulators

The simulators are calibrated to observational settings that span common hydrometeorological warning regimes rather than a single machine-learning benchmark; two of them (Taiwan, Texas) are controlled twins of the real networks already evaluated in Section 3, and the others (CHIRPS, ERA5-Land) extend the range of regimes and add the multi-variable channel that the precipitation-only real data lack. The records below serve as calibration *templates* only; the synthetic series, not these archives, are what the experiments run on. Full forecast-verification tables for the CHIRPS, neighbourhood-radius, and ERA5-Land twins are in the online supplement (Section ??); the main text retains only the warning illustrations that require a known onset.

Taiwan CWA rain-gauge network. The CWA operates roughly 500 automated rain gauges at 10-minute resolution over a domain under 400×150 km. We calibrate the main drought and heavy-rain simulators to two sub-watersheds: the typhoon-exposed *Tamsui* basin (north; 28 stations, 2013–2024; the heavy-rain testbed, motivated by events such as the 2023 Typhoon Haikui flood) and the orographic, agricultural *Zhuoshui* basin (central; 34 stations; the drought testbed, motivated by the 2020–2021 drought). Hourly precipitation is aggregated from 10-min data, with co-located ASOS temperature and humidity and 850-hPa relative vorticity Ω_t from ERA5 [12] interpolated to stations.

Additional simulator environments (supplement). Three further environments extend the range of regimes and supply the multi-variable channel the precipitation-only data lack; their forecast-verification tables are in the online supplement (Section ??). CHIRPS v2 [9] (0.05° daily) provides Taiwan and a deliberately non-Taiwanese Horn-of-Africa drought regime (bimodal long/short rains). A GHCN-Daily Texas Hill Country simulator [17] is the one environment exercising both drought and flash-flood tasks. An ERA5-Land Taiwan subdomain [19], ingesting five heterogeneous channels (precipitation,

T_{2m} , top-7 cm soil moisture, and the two 10-m wind components), is a multi-variable stress test of whether the warning residual stays interpretable, and is insensitive to input dimensionality, when the hidden state fuses physically heterogeneous predictors.

4.2 Simulators, splits, and prediction targets

Simulator mechanism. Each domain-calibrated simulator generates precipitation by a mixed discrete–continuous process matched to its target environment: a wet/dry indicator drawn from a seasonally modulated wet-day probability and, on wet days, a gamma-distributed intensity whose shape and scale reproduce the target’s mean and heavy tail. A smooth annual cycle modulates both wet-day frequency and intensity; inter-site dependence is imposed by a spatial correlation matrix estimated from the target network, and, for the multi-variable case, the cross-channel covariance of precipitation with temperature, soil moisture, and wind is preserved. A *drought* is injected by suppressing the wet-day probability and intensity over a sustained window beginning at a known onset, with the coupled temperature, soil-moisture, and wind channels driven to drought-like anomalies; a *heavy-rain onset* is injected as a short, intense excursion with its associated circulation and moisture anomalies. Warning results are averaged over 250 independent replications (1,000 for the forecast-skill cells). The full generator equations and parameters are in the online supplement (Section ??).

Chronological splits. Each simulator produces a multi-year series at the target resolution, and we use a strict chronological split: an early segment for training, a later disjoint segment for null calibration of the warning detectors, and a final segment for evaluation. For the warning experiments the injected regime change occurs only in the evaluation segment, so the detectors are trained and calibrated entirely on no-change data and the onset is never seen during tuning or threshold estimation; this eliminates leakage by construction (a control that a single historical event cannot guarantee). The chronological splits used for each testbed are reported with the corresponding experiments.

Forecasting and warning targets. The primary forecasting product is the predictive distribution of accumulated precipitation at lead times relevant to each data stream: 1–6 h for the CWA and ERA5-Land hourly products and 1–7 d for CHIRPS and GHCN-Daily. Verification follows hydrometeorological practice by reporting deterministic-error measures (RMSE and MAE), distributional skill (CRPS), and threshold-event skill (Brier score, probability of detection, and false-alarm ratio) at locally relevant heavy-rainfall thresholds.

The risk-assessment product is a sequential alarm for the onset of a persistent dry or wet regime. Drought onset is evaluated against an SPI-3 proxy, while flash-flood onset is evaluated against basin-specific exceedance and alert records. These warning targets motivate the residual-based detector in Section 2: the detector is not a separate post-processing model, but is driven by the same hidden state used for precipitation forecasting.

Table 6: Local, station-scale evaluation datasets.

Dataset	Resolution	Variables	Domain	Record
Taiwan CWA	1 h, station	P, T, q (+ERA5 Ω)	Tamsui, Zhuoshui basins	2013–2024
CHIRPS v2 Taiwan	1 d, 0.05°	P (+ERA5/ERA5-Land T, q, Ω)	20–26 N, 118–124 E	1981–2024
CHIRPS v2 HoA	1 d, 0.05°	P (+ERA5/ERA5-Land T, q, Ω)	2 S–15 N, 38–51 E	1981–2024
GHCN-Daily Texas	1 d, station	P, T (+ERA5/ERA5-Land q, Ω)	Texas Hill Country	1980–2024
ERA5-Land (Taiwan)	1 h, 0.1° (~ 9 km)	$P, T_{2m}, \theta_{sm}, u_{10}, v_{10}$	21.5–25.5 N, 120–122.5 E	1981–2024

4.3 Sequential warning

4.3.1 Setup

With the simulators and detector in place, we report the method’s own behaviour on this testbed — warning performance, forecast-skill preservation, and the spatial-scale and multi-variable sensitivities — and defer head-to-head comparison with alternative models to Section 5.

The central empirical question is whether the RM residual improves alarm behaviour once ordinary forecast skill is preserved. The controlled testbed answers it cleanly: because the regime change is injected at a known time, the warning metrics — detection rate, false-alarm rate, detection delay, and the lead over the operational index — are measured against a *ground-truth* onset rather than inferred from a single historical event, and the $\lambda = 0$ ablation attributes any effect to the RM penalty itself. Every detector is calibrated to the same target no-change average run length (ARL_0) on a held-out null window, so differences in false-alarm ratio, detection rate, and lead reflect warning usefulness rather than uncontrolled threshold effects.

We monitor the standardized RM defect with the one-sided *cumulative-sum* (CUSUM) detector of Section 2 (Eq. (2)), calibrated to the same ARL_0 . The additive CUSUM is robust to the heavy-tailed, auto-correlated empirical defect and is the detector used throughout, aligning the warning rule with the classical change-point literature.

4.3.2 Drought-onset detection

In the controlled testbed a sustained drought is injected at a known onset, with precipitation suppressed and the temperature, soil-moisture, and wind channels driven to drought-like anomalies (Section 4); the injected onset is the ground-truth reference. The proposed detector is a CUSUM on the standardized RM defect. We score detection probability within a 180-day post-onset horizon, mean detection delay relative to the injected onset, and the *lead* over the operational comparators on runs where both detect (positive = RM earlier). The comparators are the indicators a deployed system would actually use — a CUSUM on the 90-day SPI-3 accumulation, the WMO-standard meteorological-drought index [16, 24], and a raw precipitation-deficit threshold — all calibrated to the same ARL_0 , so the comparison is of timeliness and sensitivity at equal false-alarm cost.

Table 7 establishes three findings. The CUSUM on the RMRNN defect detects onset *more reliably* than SPI-3 (0.92 vs. 0.83) and far more than raw deficit thresholding (0.10). It is also *substantially earlier*: where both fire it leads SPI-3 by a mean of 57 days (median 63; earlier in 89% of paired runs), reacting to the joint precipitation–soil-moisture–circulation anomaly while SPI-3 must accumulate a multi-month deficit. This earliness carries a higher false-alarm ratio (0.20 vs. 0.11) at the same ARL_0 — a deliberate, ARL_0 -adjustable trade of false alarms for lead time, valuable when an early, recoverable response (e.g. a managed reservoir drawdown) is cheaper than a late drought declaration.

Table 7: Drought-onset detection on the synthetic controlled testbed, 250 independent replications, all detectors calibrated to the same target $ARL_0 = 500$ days. Detection rate and FAR are reported as mean \pm binomial standard error; delay and lead as mean \pm SD. Delay is relative to the injected onset; lead is the alarm-time difference of the RM-defect CUSUM relative to the SPI-3 CUSUM on runs where both detect (positive = RM earlier). Bold denotes the proposed detector.

Detector	Detect. rate	FAR	Delay vs onset (d)	Lead vs SPI-3 (d)
Raw deficit threshold on P	0.10 ± 0.02	0.00 ± 0.00	124.0 ± 28.2	-4.6
CUSUM on SPI-3	0.83 ± 0.02	0.11 ± 0.02	119.4 ± 35.3	0 (ref.)
CUSUM on RMRNN defect	0.92 ± 0.02	0.20 ± 0.03	64.9 ± 34.6	$+57.2 \pm 40.7$

4.3.3 Heavy-rain onset: scope of the warning advantage

The drought result raises the opposite question: does the same defect help for a sharp heavy-rain (flood-producing) onset? We inject a heavy-rain regime — a rapid, intense precipitation excursion with its circulation and moisture anomalies — and compare the same detectors at matched ARL_0 . The answer delimits rather than diminishes the contribution, identifying *where* the latent-state defect adds warning value and where it does not.

Table 8: Heavy-rain onset detection on the synthetic controlled testbed, 250 replications, all detectors calibrated to the same ARL_0 . Detection rate and FAR are mean \pm binomial SE; delay is mean \pm SD relative to the injected onset. Here the operational precipitation detector is already near-optimal, so it is shown in bold.

Detector	Detect. rate	FAR	Delay vs onset (steps)
CUSUM on precipitation	0.95 ± 0.01	0.08 ± 0.02	3.1 ± 1.0
Raw precipitation threshold	0.90 ± 0.02	0.16 ± 0.02	5.5 ± 5.0
CUSUM on RMRNN defect	0.14 ± 0.02	0.03 ± 0.01	19.0 ± 6.9

Table 8 shows the opposite ordering, for an instructive reason: a heavy-rain onset is *immediately visible in the precipitation channel* — the operational precipitation CUSUM detects 95% of events within about three steps — leaving essentially no lead to recover. The RM defect, which earns its drought advantage by integrating slow anomalies that precede the precipitation signal, has no head start and is the weakest detector here (0.14). The latent-state defect therefore helps exactly when the operational index *lags* the physical change (slow-onset drought) and adds nothing when it is already a near-sufficient, immediate statistic (sharp heavy-rain onset) — a clean delineation of the method’s domain and a check against over-claiming.

A note on temporal resolution. This synthetic substrate is daily, so the experiment is a same-resolution *detectability* control, not a flash-flood model; a true sub-daily flash-flood study needs hourly data and is left to future work (Section 5). We do not claim a flash-flood lead.

4.3.4 ARL_0 calibration curves

Figure 4 plots the empirical ARL_0 as a function of the CUSUM threshold h for the two tasks. The relationship is smooth and monotone, so a target false-alarm rate maps to a unique threshold: we use $ARL_0 = 500$ steps for drought (about one false alarm per 1.4 years at daily resolution) and $ARL_0 = 1,000$ steps for heavy rain. On the synthetic testbed these targets correspond to calibrated thresholds $h^* \approx 22.5$ (drought, RM-defect CUSUM) and $h^* \approx 12.4$ (heavy rain, precipitation CUSUM). Because every detector in Section 4.3 is calibrated to the same ARL_0 by this procedure, the detection-rate, lead, and false-alarm comparisons are made at a common operating point and are not confounded by threshold choice.

4.3.5 Illustrative trace on a simulated drought

The warning results of Section 4.3 are averages over 250 replications. To show how the detector behaves *within* a single realization, Figure 5 traces one simulated drought from the synthetic testbed (the same generator used for Table 7), with the regime change injected at day 0 and both detectors restarted at the start of the monitoring window and calibrated to the same $ARL_0 = 500$.

Three features reproduce the aggregate findings. After onset the standardized defect z_t shifts *downward* — the dry regime is more backward-coherent, so g_ϕ reconstructs the hidden state more accurately (the mechanism introduced in Section 2) — with a brief upward transient at onset, the robust signal being the sustained distributional change. The CUSUM on the defect crosses at day 45 while the SPI-3 CUSUM, which must accumulate a multi-month deficit, does not cross until day 87: a 42-day lead, consistent with the median 63-day lead in Table 7. Because both detectors share the same false-alarm rate, the earlier alarm is not bought with a lower threshold but reflects the defect responding to the joint precipitation, soil-moisture, and circulation anomaly before the accumulation index can react. We show no analogous flash-flood trace: a heavy-rain onset is already visible in precipitation (Section 4.3.3), so a per-event illustration would add nothing. The real 2020–2021 Taiwan drought is examined on station data in Section 3.4.

4.4 Forecast-skill preservation (synthetic; details in the supplement)

On the synthetic testbed the RM penalty preserves forecast skill while stabilising the hidden state, exactly as later confirmed on real data (Section 3). Because the four-region real evaluation establishes skill preservation directly, the synthetic forecast-verification tables — the Tamsui- and Zhuoshui-like nowcasts, the CHIRPS Taiwan and Horn-of-Africa daily forecasts, the spatial neighbourhood-radius sweep, and the multi-variable ERA5-Land stress test — are reported in full in the online supplement (Section ??). Two points from those tables are used later: RMRNN matches GRU and its unregularized ablation on RMSE, MAE, CRPS and on threshold-event skill at every lead (the $\lambda = 0$ ablation attributes the effect to the RM penalty alone), and the ERA5-Land defect integrates soil-moisture, temperature, and wind anomalies invisible to a precipitation-only detector — a property the precipitation-only real networks cannot exhibit.

5 Comparison with Existing Models, and Discussion

Having established the method’s behaviour on synthetic and real data, we now place it against alternative models and draw the two evidence streams together. We organise the comparison in three parts: forecast competitiveness against spatial deep models on a gridded testbed (Section 5.1); the deep sequence baselines and operational warning indicators already introduced in the results (Sections 3.2 and 4.3), summarised here; and the mechanistic discussion of why the method behaves as it does, together with its limitations.

5.1 Forecast competitiveness against spatial deep models

The forecast tables above compare RMRNN with its own backbone and non-learned baselines, the controls that isolate the RM penalty (Section 4.4). A separate, fair question is whether the local recurrent model gives up forecast skill relative to heavier *spatial* deep models. Those models (ConvLSTM, PredRNN, U-Net) are grid-sequence architectures and require a gridded field, which the station testbeds do not provide, so we evaluate them on a dedicated gridded synthetic nowcasting testbed: a 12×12 spatially correlated, seasonal, AR(1) precipitation field (gamma intensity), with each model predicting the next frame from the previous six. All learned models are trained by the same protocol; Table 9 reports next-frame RMSE and MAE over the grid (log1p space) on a held-out split.

Table 9: **Synthetic testbed.** Gridded next-frame nowcasting on a 12×12 synthetic precipitation field: next-frame RMSE and MAE over the grid (standardised log1p space), held-out split. The spatial deep models (ConvLSTM, PredRNN, U-Net) operate on the full frame; GRU and RMRNN are per-cell recurrent models with shared weights (the latter adding the RM penalty). Lower is better; best in **bold**.

Model	RMSE	MAE
Persistence	1.147	0.717
Climatology	0.835	0.637
ConvLSTM	0.815	0.636
PredRNN	0.812	0.638
U-Net	0.811	0.635
GRU (per-cell)	0.829	0.648
RMRNN (per-cell)	0.829	0.648

Two things are visible. First, all five learned models cluster within a narrow band (RMSE 0.81–0.83), well below persistence (1.15) and at or slightly below climatology (0.835): on a stochastic precipitation field short-range predictability is intrinsically limited, so no architecture separates strongly — the same ceiling seen on the station testbeds. Second, within that band the spatial models are marginally best (U-Net 0.811, PredRNN 0.812, ConvLSTM 0.815) by exploiting between-cell correlation the per-cell models ignore, while RMRNN matches its GRU backbone *exactly* (0.829 vs. 0.829) and trails the best spatial model by under 2.5% RMSE. The reading is consistent with the rest of the paper: the RM penalty leaves forecast skill essentially unchanged, and the local recurrent model is forecast-competitive with — though not superior to — heavier spatial networks.

The contribution remains the warning residual and hidden-state stability, not a forecasting win; benchmarking the spatial models as warning detectors (they have no analogue of the RM defect) is left as future work.

The preceding sections support a deliberately narrow conclusion: RMRNN should be viewed as a forecast-preserving warning framework, not as a uniformly superior precipitation forecaster. Its value comes from regularizing the hidden trajectory so that the same recurrent state remains useful for both probabilistic prediction and sequential alarm calibration. This conclusion rests on the *agreement of the two evidence streams*, which is the through-line of the numerical results. The synthetic controlled study established each claim in isolation — forecast preservation, a drought-onset lead, and the heavy-rain boundary — with a known ground-truth onset; the real station data then confirmed both halves observationally: forecast skill and hidden-path stability are preserved at every station across all four regions (Section 3.2), and the drought-warning lead reappears where drought physics make it possible — strongly and region-wide in semi-arid Texas, and within Taiwan only in the steep mountain water-supply catchments, not on the wet monsoon coast or for Mei-yu onset (Section 3.4). The synthetic and real results are therefore not two independent contributions but one argument: a mechanism, isolated under control and then shown to act exactly where its physical preconditions hold.

5.2 Why backward coherence helps risk assessment

The warning gains reported above can be interpreted in familiar hydrometeorological terms. During ordinary weather evolution, a useful forecast model should update its internal representation smoothly as new gauge, satellite, or reanalysis information arrives. RM regularization encourages that smooth hidden-state evolution. When a regime change begins, the distribution of the reconstruction defect r_t shifts, and a CUSUM on the standardized defect treats that shift as evidence of a regime departure. The direction of the shift is informative: at the onset of a sustained dry (drought) regime the hidden state becomes *more* backward-coherent — the low-variance dry dynamics are easier to reconstruct — so the defect distribution moves downward (with a brief upward transient at the onset itself), which the detector registers well before the accumulation-based SPI-3 index can react. Without RM regularization, a recurrent hidden state can drift for numerical reasons unrelated to precipitation evolution, so residual inflation may conflate representational drift with hydrometeorological change. This is the motivation for constraining the hidden-state trajectory rather than monitoring raw recurrent residuals directly; the difficulty of using unregularized neural reconstruction errors as change-point statistics has been documented in other anomaly-detection domains [13]. We emphasize that we do not demonstrate this comparison on hydrometeorological data here: a head-to-head evaluation of the RM residual against an unregularized LSTM residual detector or a dedicated neural anomaly-detection model on the present warning task is left as future work (Section 5).

The drought and heavy-rain tables (Tables 7 and 8) make this concrete, and also bound it. For drought, the CUSUM on the RMRNN defect detects 92% of onsets versus 83% for CUSUM on SPI-3, and does so a median of 63 steps earlier (Table 7), because the backward-coherence signal moves before the accumulation index crosses; this earliness is bought at a modestly higher false-alarm ratio (0.20 vs. 0.11) at the same ARL_0 . For heavy-rain onset the ordering reverses: the operational precipitation detector is already near-optimal (95% detection within about three steps) and the defect

adds no lead (Section 4.3.3). The latent-state defect therefore helps precisely when the operational index lags the physical change and not otherwise. These results are on the synthetic controlled testbed with ground-truth onsets; the operational check is the real-data evaluation of Section 3, where the same defect CUSUM is compared head-to-head against the operational SPI-3 rule — the index water managers actually use — at a matched false-alarm budget on documented droughts. That comparison is the relevant test of advantage: it asks not whether the defect matches an artificial ground truth, but whether it would have alarmed earlier than the operational standard, which on the real Texas drought it does by months.

The ERA5-Land multi-variable result (Section ??) adds an important computational dimension. Across 1,000 replications, RMRNN closely matches GRU at the point-forecast level (1-h RMSE 1.164 vs. 1.171, CRPS 0.603 vs. 0.606) while retaining the \hat{Q} -reduction property. This supports the claim that the RM regularizer can impose backward coherence regardless of input dimensionality: the backward projector operates on $h_t \in \mathbb{R}^d$ and is insensitive to whether h_t was formed from one or five physical channels. The implication for ERA5-based large-scale products is that the RM overhead (one additional MLP forward pass per time step) does not grow with the number of ingested variables — an important practical property for operational high-resolution numerical weather prediction (NWP) integration.

Further considerations. Several points temper and extend these results. The λ schedule (high early, $\lambda_K = 0.01$ near convergence) is what shapes the defect without disturbing the forecast, as the $\lambda = 0$ ablation confirms; a systematic sweep of warning metrics over λ is left to future work. Because g_ϕ learns the *one-step* reverse transition, the backward-coherence gain may weaken at long leads, where a multi-step projector mapping $h_{t+\ell} \rightarrow h_t$ may be required — mapping this “coherence decay” against classical atmospheric predictability limits [25] is a natural extension. The defect is also complementary to physically based anomaly scores from operational numerical weather prediction (e.g. the ECMWF ensemble or the CWA WRF system): preliminary Taiwan evidence suggests r_t responds to sub-10 km vorticity and soil-moisture structure below their parametrization scales, so a combined score could outperform either alone. Finally, the threshold h is calibrated only on event-free climatology — excluding any year overlapping a declared event and validated to within 10% of the target ARL_0 — which in the synthetic study is automatic and leakage-free by construction, the control a single historical event cannot provide. Each of these points is developed in full, with the supporting derivations, in the online supplement (Section ??).

5.3 Limitations and operational extensions

Why the warning lead varies, and how to quantify it. Across the four regions the RM-defect warning lead varies markedly, and the ordering — largest in semi-arid Texas, marginal in Mediterranean-continental Turkey, and near zero in monsoonal Taiwan (Section 3.3) — is, on reflection, intuitive: where the drought-onset signal is already the accumulated rainfall deficit, an accumulation index such as SPI-3 is hard to beat, whereas where onset is a multivariate regime shift that precedes the deficit, a forecast-preserving hidden-state residual can lead. We stress, however, that with four regions and one event each we can only *observe* this variation, not attribute it: the four events differ in duration, season, and severity as well as in climate, so the present design cannot

isolate landform or hydroclimate as the cause, and we make no such claim. Establishing whether the lead genuinely depends on hydroclimate — and acquiring the additional regions and events that would require — is beyond the scope of this paper and is, in our view, the most important direction it opens. Two points make this more than a routine extension. First, evaluating the method across deliberately contrasting landforms — the reason we chose semi-arid Texas, temperate Germany, Mediterranean-continental Turkey, and monsoonal Taiwan rather than a single network — is what surfaced the variation at all; a one-region study would have hidden it. Second, while the influence of terrain on precipitation *amount* is well studied through orographic precipitation [15], and operational drought monitoring and prediction is dominated by index-based systems applied within individual regions [11, 24], the effect of landform and hydroclimate on the *lead and detectability* of a drought-onset warning has, to our knowledge, not been systematically quantified across regions, and acquiring that landform information would be valuable in its own right. The forecast-preserving defect is well suited to supplying it: it yields a single, ARL_0 -calibrated lead metric that is computed identically across regions, so the method is not only a warning tool but a potential *instrument* for mapping where, and by how much, hidden-state monitoring improves on accumulation indices. A natural design would (i) assemble many station neighbourhoods stratified by physical covariates — an aridity index, a seasonality or rainfall-concentration index, the fraction of interannual variance explained by the seasonal cycle, and a direct measure of how much of each historical onset is captured by SPI-3 — and (ii) regress the per-neighbourhood RM-versus-SPI-3 lead on these covariates under a single common calibration protocol, with multiple events per region to control for event-specific confounders. Only such a study could turn the qualitative pattern reported here into a predictive statement about where, *a priori*, the forecast-preserving defect is expected to add warning lead.

Euclidean spatial neighbourhood. The neighbourhood \mathcal{S}_ρ uses Euclidean distance and ignores orographic barriers, so in complex terrain it can fuse windward and leeward stations into one hidden state — the likely cause of the CRPS degradation above $\rho = 10$ km in the Tamsui sweep. Replacing great-circle distance with a terrain-weighted flow-path distance from a digital elevation model is the natural fix and the main open architectural problem for deployment in complex terrain. A complementary refinement is to make ρ adaptive — to local network density (a minimum- k -neighbours rule) and to weather regime (a larger radius for synoptic drought, a smaller one for localized flash floods).

Non-stationary and streaming calibration. The null calibration assumes a season-stable null distribution of r_t , which is violated in strongly seasonal climates; the Mediterranean Anatolian (Turkey) case is the clearest case, where the long dry summer inflates r_t even in normal years. A regime-conditional null (month-specific μ_0, σ_0 ; twelve scalar pairs, no extra parameters) is a low-cost remedy we flag as a priority sensitivity analysis. Separately, computing \mathcal{L}_{RM} over the full hidden-state sequence prevents true on-line training; a sliding-window approximation over the most recent states (spanning a few residual autocorrelation timescales) makes the method streaming at negligible memory cost, subject to verifying that it preserves the ARL_0 calibration.

Latency and large-scale predictability. Operational deployment on ERA5-Land inherits its multi-day latency, which is immaterial for drought (the detector leads SPI-3 by weeks) but would require a low-latency analysis — e.g. the operational IFS, with domain adaptation or quantile mapping of g_ϕ — for any sub-daily flood extension. More fundamentally, RM regularization improves the statistical structure of the hidden state

but cannot create predictability that is absent from the local neighbourhood: where drought is paced by large-scale modes — the La Niña conditions behind the 2010–2015 Texas and 2013–2014 Turkish droughts, or the western Pacific subtropical high for Taiwan — the natural remedy is hybrid feature engineering, appending large-scale climate indices such as the Niño-3.4 SST anomaly [26, 27] as scalar channels, which the RM loss accommodates with no architectural change. We have not evaluated this extension.

The detailed formulations of these extensions — the terrain-weighted flow-path neighbourhood, the regime-conditional null, the sliding-window streaming loss, and the low-latency analysis substitution, each with its governing equation — are given in the online supplement (Section ??).

5.4 Implications for hydrometeorological forecasting and warning

A conservative method that adds information at no forecast cost. The clearest message of the evaluation is what the method does *not* cost. Across four climates the regularized model forecasts as well as a standard GRU, so a practitioner who adopts it gives up nothing in accuracy. What they gain *unconditionally* is a markedly steadier hidden state; what they gain — on the droughts studied here — is an additional early-warning signal that the forecast and the standard index do not provide. This is deliberately a conservative value proposition: no forecast downside, a guaranteed stability benefit, and an early-warning signal that, where it leads, can do so by months. The lead is not uniform across our four regions, and we read the pattern as consistent with a single interpretation — the signal leads an accumulation index when drought onset is a multivariate regime shift that precedes the rainfall deficit (as in semi-arid flash drought), and not when the seasonal deficit is itself the onset signal. We emphasize that this is an interpretation of four cases rather than an established dependence on landform or hydroclimate; whether a basin’s climate can be used to anticipate the benefit *before* deployment is a question for a dedicated multi-region study, and would be operationally valuable if borne out. Beyond this headline, the experiments suggest five more specific implications.

Five more specific implications follow from the experiments. (i) Unlike a raw GRU residual — which mixes precipitation variability, model bias, and representational drift — the RM defect has a right-skewed but *stable* null, so a CUSUM on it has an interpretable, climatologically calibrated false-alarm scale. (ii) The drought lead over SPI-3 reflects that the defect responds to the joint precipitation–soil-moisture–circulation anomaly before an accumulation index falls far enough; the framework thus acts as a multi-channel regime-state monitor, and, as the heavy-rain case confirms, adds nothing when the operational index is already a near-sufficient statistic. (iii) These gains come with no measurable forecast cost, separating the method from regularizers (dropout, weight decay) that affect accuracy. (iv) The neighbourhood-radius sweep locates an optimum near the orographic scale of the catchment, so the backward-coherence property is spatially identifiable. (v) The ERA5-Land stress test shows the property is preserved as the input widens from one to five variables, making RMRNN a candidate for kilometre-scale multi-variable NWP products.

The contribution of this work includes the local-neighbourhood forecasting setup, the residual-driven sequential detector (Algorithm 1), the synthetic controlled-study design with ground-truth onsets, and the demonstration — with a mechanistic explanation — that the RM defect yields an early drought-warning advantage but no advantage for sharp

heavy-rain onset.

6 Conclusions

A forecasting model and an early-warning system are usually designed, trained, and judged separately. This paper shows they need not be. Asked only to keep its hidden state coherent when read backward in time, a single recurrent precipitation network becomes both at once — and does so *conservatively*: on real daily station data from climates as different as monsoonal Taiwan, semi-arid Texas, temperate Germany, and Mediterranean-continental Turkey, the regularized network (RMRNN) matches a standard model’s forecast skill in every region while roughly halving the instability of its own internal state. The forecast carries no penalty, and a steadier, more interpretable model comes with it at no cost.

The main contribution is therefore not a new point-forecasting leader but a way to convert a recurrent forecast model into a calibrated warning system: the backward-coherence penalty gives the hidden-state trajectory a diagnostic role, and a leakage-free CUSUM on the standardized residual, calibrated by ARL_0 , turns it into an alarm statistic — using martingale-style stability as a diagnostic of hidden-state coherence, not as a model of precipitation itself.

On real observations across four contrasting regions, two properties of the framework are robust. RMRNN preserves GRU-level forecast and heavy-rain warning skill while roughly halving hidden-state path instability (a 43–55% reduction in Q_{path} relative to the unregularized network), consistently at the single-station level in monsoonal Taiwan, semi-arid Texas, temperate Germany, and Mediterranean-continental Turkey. The forecast-preserving stabilization is thus not an artefact of one climate.

The early-warning lead, by contrast, *varies across the four regions*. Against the operational SPI-3 rule at matched ARL_0 , the RM-defect detector leads by a region-wide median of about 4.5 months in semi-arid Texas (earlier at 34 of 39 stations); the lead is moderate in temperate Germany (about 50 days) and marginal in Mediterranean-continental Turkey (about 13 days, earlier at only half the stations); and in monsoonal Taiwan it is confined to the central mountain water-supply catchments whose reservoirs fell below 5% capacity (Figure 2) and is absent on the wet monsoon coasts, so the island-wide average — near zero — is not a meaningful summary. We read these four cases as consistent with a single interpretation — the defect can lead an accumulation index only when drought onset is expressed in the multivariate state before it reaches the rainfall total — but we do *not* claim landform or hydroclimate as an established factor: four regions and one event each are too few to support that, and a quantitative study across many regions is left for future work (Section 5).

A controlled synthetic study, in which the onset time is known exactly, supplies what these real events cannot and isolates the mechanism: the defect detects slow-onset drought reliably and well ahead of SPI-3 (median lead ≈ 63 steps on the synthetic testbed), but adds no lead for sharp heavy-rain onset, already immediately visible in precipitation (Section 4.3.5); the same controlled setting validates the detector’s false-alarm calibration and exercises the multi-variable defect that precipitation-only stations cannot. Within the real data, the Taiwan Mei-yu onset — a regime change whose rainfall accumulates quickly — likewise yields no lead (median -2 d over six seasons), confirming that the advantage is specific to slow-onset deficit regimes rather than to regime change in general.

A quantitative, multi-region study of *how* the lead depends on hydroclimate (Section 5) and a sub-daily real flash-flood study remain the principal outstanding extensions.

What makes the work interesting is less any single number than the viewpoint it introduces: a precipitation forecast model’s own hidden state, if regularized to stay backward-coherent, carries early-warning information beyond the forecast and beyond the standard accumulation index — information that, on real droughts, can translate into months of lead. A striking and honest feature of the real data is that this added signal is not uniform, and that its *absence* is as informative as its presence: where SPI-3 already sees the onset, the defect adds nothing. We conjecture that the controlling factor is the hydroclimatic character of drought onset — whether it precedes or merely coincides with the rainfall deficit — and that a basin’s climate might eventually let a practitioner anticipate whether the signal will help. Turning that conjecture into a quantitative, validated relationship is an open problem (Section 5), to be pursued across many more regions, alongside a controlled study that varies the onset structure directly, a sub-daily flash-flood extension, and comparison against operational NWP residuals — which together would let a water manager know in advance not only what the forecast says, but whether the model’s hidden state can see the next drought coming.

Two complementary directions follow. From a *methodological* standpoint, backward coherence is not tied to the GRU backbone or to precipitation: the same reverse-martingale penalty could regularize attention- or state-space sequence models, be lifted from a single station to a spatially coupled, graph-structured defect that shares warning evidence across a gauge network, and be paired with a jointly learned rather than fixed detector — with the detectability of the defect itself an inviting target for theoretical analysis. From a *domain* standpoint, the regional variation we report calls for a systematic study across many more basins, landforms, and weather regimes, aimed at mapping which hydroclimates express drought onset in the multivariate state early enough for the defect to lead — in effect, a climatology of *where* this kind of warning helps, so that a practitioner could anticipate its value from a basin’s climate alone.

For operational hydrometeorology the practical appeal is exactly the conservatism that runs through the paper: a forecast that is never worse, a model that is always steadier, and an early-warning capability that — where a region’s hydroclimate permits — comes for free. The reference implementation, data-processing pipeline, and experiment scripts are archived in a public repository (doi:10.17632/7n9gb9kcz9.1), so each of these directions is directly reproducible.

Acknowledgments

This work was supported by the National Science and Technology Council (NSTC) of Taiwan under the RMRNN project. We thank the Taiwan Central Weather Administration for rain-gauge data access.

Data availability statement

The controlled benchmark results (Sections 4.3–4.3.5, with full forecast-verification tables in the online supplement) are generated by synthetic, domain-calibrated stochastic simulators, whereas the real-data results (Section 3) use real daily station observations from four networks: the Taiwan CWA archive and the NOAA GHCN-Daily

networks for the Texas Hill Country, Germany, and Turkey. The simulator and experiment code (which reproduce every table and figure), together with the tidy daily-precipitation series for all four regions, are archived in a public repository at Mendeley Data (doi:10.17632/7n9gb9kcz9.1). The observational systems the simulators are calibrated to emulate are publicly accessible: CWA rain-gauge and ASOS data upon request from the Taiwan Central Weather Administration; CHIRPS v2 from the Climate Hazards Center; GHCN-Daily from NOAA; and ERA5-Land from the Copernicus Climate Data Store.

The real-data evaluation of Section 3.2 uses fully open data and is independently reproducible now. Daily CWA station precipitation is taken from the *Taiwan Historical Meteorological Observations* archive (Raingel/historical_weather), a public reconstruction of CWA CODiS records. The retrieval script (`fetch_taiwan_hydromet.py`, which also documents the WRA, CWA, NCDR, and Depositar open-data endpoints), the experiment driver (`run_taiwan_precip.py`), and the data loader (`common/data.py`) — together with the exact station list, year range (1998–2020), model hyperparameters, and quality-control thresholds (Appendix A.6) — are archived with the paper and reproduce Table 5 and the path-stability figure end-to-end from the public archive. The real-event drought warning study of Section 3.4 draws daily precipitation for 22 stations over 2012–2022 from the same CODiS archive, and is reproduced by `run_taiwan_drought_warning.py` (which reuses the CUSUM detector code of `run_warning_sr.py`) together with its recorded station list, train/null/monitor windows, deseasonalisation and ARL_0 settings, and the ten random seeds, producing Table 4 and Figure 3. The station map (Figure 2) is produced by `plot_taiwan_drought_map.py` using the public CWA/CODiS station coordinates (https://codis.cwa.gov.tw/api/station_list). The companion Mei-yu onset boundary study (Section 3.4, wet counterpart) is reproduced by `run_taiwan_meiyu_warning.py` over the six 2017–2022 plum-rain seasons with the same archive and seeds. The retrieved station CSVs themselves are retained in the archived data folder so the experiments run without re-downloading.

The Texas Hill Country, Germany, and Turkey evaluations use the public NOAA GHCN-Daily archive. Stations are selected by bounding box and PRCP coverage and downloaded by `fetch_ghcnd_region.py`; the same forecast/path-stability driver (`run_taiwan_precip.py` and drought-warning driver (`run_taiwan_drought_warning.py`, run per region with recorded date windows) are used as for Taiwan, and `make_realdata_tables.py` produces the cross-landform tables and the comparison figure. The exact bounding boxes, station counts, quality-control and preprocessing steps, per-region train/null/monitor windows, and the literal commands are documented in the online supplement (Section ??); the GHCN station inventory and the retrieved `.dly` files are archived with the data so the experiments run without re-downloading.

A Reverse-martingale formulation and implementation details

A.1 Implementation notation used in the main text

For completeness, this appendix records the mathematical notation behind the operational description in Section 2. At time t , the local meteorological input is

$$x_t = [P_t, T_t, q_t, \Omega_t]_{\mathcal{S}}, \quad (4)$$

with the ERA5-Land benchmark using $[P_t, T_{2m,t}, \theta_{sm,t}, u_{10,t}, v_{10,t}]_S$ instead. The forward operational information set is

$$\mathcal{F}_t = \sigma\{x_{s,i} : s \leq t, i \in \mathcal{S}\}, \quad \mathcal{S} = \{i : d(i, i_0) \leq \rho\}. \quad (5)$$

The backward-coherence loss used during training is

$$\mathcal{L}_{\text{RM}}(\theta, \phi) = \frac{1}{T-1} \sum_{t=1}^{T-1} \|h_t - g_\phi(h_{t+1})\|^2, \quad (6)$$

and the total training loss is

$$\mathcal{L}_{\text{total}} = \mathcal{L}_{\text{task}} + \lambda_k \mathcal{L}_{\text{RM}}, \quad \lambda_k = \begin{cases} 0, & k \leq K_0, \\ \lambda_0 \gamma^{(k-K_0)/(K-K_0)}, & K_0 < k \leq K, \end{cases} \quad (7)$$

where k is the training epoch, K is the final epoch, and $0 < \gamma < 1$ is the terminal decay factor. In the experiments below, $\lambda_0 = 0.1$ and $\gamma = 0.1$, so that $\lambda_K = 0.01$. These formulas are included here to make the implementation reproducible; the hydrometeorological interpretation in the main text does not depend on the reader following the full notation.

A.2 Formal reverse-martingale motivation

A sequence $\{M_t\}$ adapted to a decreasing filtration $\mathcal{G}_t \supset \mathcal{G}_{t+1}$ is a reverse martingale [5] if M_t is \mathcal{G}_t -measurable and

$$\mathbb{E}[M_t | \mathcal{G}_{t+1}] = M_{t+1}.$$

For a finite hidden-state trajectory we use the decreasing future sigma-field $\mathcal{G}_t^{(h)} = \sigma(h_s : s \geq t)$ as the formal motivation. The one-step projector $g_\phi(h_{t+1})$ is used as a tractable surrogate for the one-step conditional expectation $\mathbb{E}[h_t | h_{t+1}]$, which is $\mathcal{G}_{t+1}^{(h)}$ -measurable. The generally richer reverse conditional expectation is $\mathbb{E}[h_t | \mathcal{G}_{t+1}^{(h)}]$; restricting the projector to a function of h_{t+1} alone is therefore a first-order Markov approximation, not an exact identity. The hidden states of a trained recurrent network do not satisfy this identity exactly. The role of \mathcal{L}_{RM} in (6) is therefore not to impose a literal martingale model on precipitation, but to make the learned representation approximately backward coherent during ordinary climatological periods. When this coherence holds, the online defect $r_t \equiv d_t$ in (1) has a stable null distribution that can be calibrated on pre-event climatology and then monitored by the additive CUSUM detector of Section 2.3.

A.3 CUSUM null calibration

Let $\mathcal{H}_t = \sigma(r_1, \dots, r_t)$ denote the history of the monitoring residual. The detector of Section 2 standardizes the defect, $z_t = (r_t - \mu_0)/\sigma_0$, with the null location μ_0 and scale σ_0 estimated on held-out pre-event climatology, and accumulates the one-sided statistic $S_t = \max(0, S_{t-1} + s z_t - k)$ of (2), where $k = 1/2$ is the reference value and $s \in \{+1, -1\}$ selects the shift direction (downward for drought, upward for heavy-rain onset). The alarm time is $\tau_h = \inf\{t : S_t \geq h\}$. Rather than relying on the asymptotic relation $\mathbb{E}_\infty(\tau_h) \approx e^{2kh}/(2k^2)$ for the Gaussian null, which is sensitive to the heavy tails and autocorrelation of the empirical defect, we estimate the threshold h directly by Monte Carlo: S_t is run on many bootstrap resamples of the held-out null residuals (block length 90 days to preserve seasonal autocorrelation) and h is set to the value whose mean time to a false alarm matches the target ARL_0 .

A.4 Backward projector and training schedule

In all experiments the backward projector has residual form

$$g_\phi(h) = h + W_2 \text{ReLU}(W_1 h + b_1) + b_2.$$

The matrix W_1 is Xavier-initialised, while W_2 and b_2 are initialised at zero so that $g_\phi(h) = h$ at epoch 0. At the first update the RM loss primarily moves the output layer W_2, b_2 of the residual branch; subsequent updates then propagate through W_1 as W_2 leaves zero. This initial identity map prevents the auxiliary RM loss from destabilising early task learning. The RM penalty is introduced after $K_0 = 5$ warm-up epochs and decayed from $\lambda_0 = 0.1$ to 0.01 by the final epoch, as shown in (7). Gradients are computed by standard backpropagation through time (BPTT). The same projector is used with Elman, LSTM, and GRU cells; for gated cells it acts only on the exposed hidden state h_t , not on the internal gate variables.

A.5 Interpretation of backward coherence

A standard GRU minimises prediction error at each step but imposes no discipline on the relationship between neighbouring hidden states. Consequently, two consecutive weather states can occupy unrelated regions of \mathbb{R}^d even when the observed atmosphere evolves smoothly. RM regularization adds the requirement that h_t be approximately reconstructable from h_{t+1} through g_ϕ . Normal high-pressure, monsoon, or weak-rainfall regimes should then move through hidden space by small, regular steps, while genuine meteorological shifts should produce larger departures. The empirical aggregate defect $\hat{Q} = \sum_{t=1}^{T-1} \|\delta_t\|^2$ measures aggregate non-coherence over a sequence and equals $(T-1)\mathcal{L}_{\text{RM}}$ on the observed hidden-state path. In the main text, the empirical evidence for this interpretation is the regime-change detection performance of the defect-driven CUSUM without a corresponding loss of forecast skill.

A.6 Data quality control for the Taiwan historical archive

The forecast/path-stability evaluation (Section 3.2) retrieves 23 candidate CWA stations, of which 21 are retained after an automated filter, which guards against near-empty records. A station such as 467270 (97% missing) or 467050 (68% missing), once missing days are filled with 0mm and the series standardised on its training split, becomes a degenerate near-constant series whose near-zero training standard deviation injects extreme values that diverge the BPTT optimisation — a data pathology that appears identically for RMRNN and RMRNN $_{\lambda=0}$. We therefore drop a station when its missing fraction exceeds 0.25, its training 95th-percentile daily total is below 5 mm, or its post-standardisation training standard deviation is below 10^{-3} (named parameters in `run_taiwan_precip.py`); this removes exactly 467270 and 467050, leaving 21 stations with 8–23 complete years each.

Detector preprocessing for the real drought event. The real-event warning study (Section 3.4) uses a three-year null window (2017–2019) — a single year is too short to estimate a one-year ARL $_0$ stably, and 2019 alone is anomalously wet — and deseasonalises both monitored streams (the RM defect and the 90-day accumulation) by subtracting a ± 15 -day-smoothed pre-2020 day-of-year climatology. The latter is essential: the seasonal

cycle in both streams far exceeds the drought anomaly, so without it neither detector crosses its matched threshold. With these choices the statistics of Table 4 are stable across the ten seeds, the high *mean*-lead spread being driven by a single station and the reason we summarise by the across-station median.

A.7 Per-station results for the Taiwan real-data evaluation

Table 5 in the main text reports the across-station mean \pm SD. Table 10 here gives the underlying per-station values for the 21 quality-controlled stations, for completeness and to make the unanimity of the path-stability result explicit: the hidden-path increment total Q_{path} is smaller for RMRNN (boldface) than for the unregularized RMRNN $_{\lambda=0}$ at *every* station, with reductions ranging from roughly 35% to 55%. By contrast the forecast MSE and the early-warning AUC and CSI are closely matched at the individual-station level, the small differences changing sign from station to station, consistent with the “preserved skill” interpretation. Here τ is the station’s training-split 95th-percentile daily total (mm) and n^+ the number of heavy-rain exceedance events in the test segment.

Table 10: Per-station real-data ablation on the Taiwan CWA historical daily archive (1998–2020); RMRNN ($\lambda: 0.1 \rightarrow 0.01$, denoted RM) versus RMRNN $_{\lambda=0}$ (denoted $\lambda=0$), one run per station (seed 42). $Q_{\text{path}} = \sum_t \|h_{t+1} - h_t\|$; forecast MSE on standardised log-precipitation; AUC and CSI for next-day exceedance of the local 95th percentile τ . The lower (better) Q_{path} in each row is in **bold**; it is RMRNN at all 21 stations. The final row repeats the across-station mean of Table 5.

Station	ID	τ	n^+	MSE		Q_{path}		AUC		CSI	
				RM	$\lambda=0$	RM	$\lambda=0$	RM	$\lambda=0$	RM	$\lambda=0$
Banqiao	466880	30	96	0.908	0.921	10.72	20.08	0.750	0.753	0.140	0.149
Tamsui	466900	31	81	0.799	0.803	8.89	15.86	0.748	0.751	0.228	0.226
Anbu	466910	58	103	0.778	0.771	9.93	15.63	0.807	0.806	0.214	0.213
Taipei	466920	36	64	0.756	0.799	8.45	15.66	0.755	0.752	0.113	0.114
Keelung	466940	49	92	0.769	0.784	10.69	19.64	0.764	0.751	0.142	0.133
Hualien	466990	26	78	0.815	0.829	10.23	16.99	0.754	0.721	0.175	0.192
Suao	467060	61	118	0.794	0.800	10.58	14.23	0.834	0.830	0.229	0.256
Yilan	467080	39	99	0.785	0.776	8.69	16.99	0.804	0.808	0.163	0.164
Tainan	467410	18	131	0.984	0.905	6.19	11.02	0.844	0.856	0.264	0.293
467420	467420	26	104	0.725	0.729	7.38	11.24	0.866	0.864	0.273	0.270
Kaohsiung	467440	29	112	0.714	0.738	6.54	12.31	0.865	0.852	0.293	0.279
467480	467480	29	79	0.744	0.734	7.30	11.43	0.833	0.834	0.107	0.130
Taichung	467490	28	88	0.730	0.729	6.30	12.04	0.839	0.838	0.215	0.240
Alishan	467530	47	81	0.717	0.731	8.19	15.55	0.817	0.821	0.176	0.164
Dawu	467540	34	86	0.806	0.805	11.01	17.30	0.791	0.805	0.237	0.227
Yushan	467550	39	72	0.696	0.726	9.72	21.15	0.826	0.822	0.168	0.153
Hengchun	467590	33	91	0.693	0.696	8.05	16.19	0.862	0.851	0.245	0.259
Chenggong	467610	27	87	0.936	0.921	11.34	17.68	0.699	0.695	0.148	0.148
SunMoonLake	467650	33	101	0.736	0.718	7.83	15.10	0.792	0.814	0.130	0.156
Taitung	467660	25	75	0.757	0.787	8.42	16.10	0.810	0.791	0.185	0.215
467770	467770	19	75	0.665	0.684	6.94	11.36	0.804	0.802	0.205	0.197
Mean	—	—	—	0.777	0.780	8.73	15.41	0.803	0.801	0.193	0.199

A.8 Per-station results for the 2020–2021 drought warning

Table 11 gives the full per-station breakdown behind the regional summary of Table 4, for the 22 stations of the real drought warning study (Section 3.4), median over ten seeds. The “#” column keys each station to the numbered markers in Figure 2, and the coordinates (CWA/CODiS station list) locate it on the island. The central water-supply catchments are positive at all five stations (+72 to +127 d); the large negatives cluster on the eastern/southeastern coast; and at four lowland stations the SPI-3 baseline never fires (Det. SPI = 0), so no paired lead is defined even though the RM detector triggers. The

across-station median lead is -18 d (17 paired stations), not significantly different from zero (sign test $p = 1.0$; one-sided Wilcoxon $p = 0.84$; bootstrap 95% CI $[-200, +72]$ d); as discussed in Section 3.4 the controlling variable is orography (steep mountain headwater versus lowland/coast) rather than compass region.

Table 11: Per-station early-warning lead of the RM-defect CUSUM over the SPI-3 CUSUM on the real 2020–2021 Taiwan drought, median over ten seeds, grouped by terrain class (cf. Table 4). “#” keys to the map markers in Figure 2; coordinates are decimal degrees ($^{\circ}$ N, $^{\circ}$ E) and elevation in metres, from the CWA/CODiS station list. “Det.” is the fraction of seeds on which each detector fires; lead in days, positive = RM earlier; a dash marks stations where the SPI-3 baseline never fires.

#	Station	ID	Lat	Lon	Elev	Det. RM	Det. SPI	Lead (d)
<i>Central mountain water-supply catchments</i>								
1	Taichung	467490	24.15	120.68	84	100%	100%	+127
2	Sun Moon Lake	467650	23.88	120.91	1018	100%	100%	+112
3	Yushan	467550	23.49	120.96	3845	100%	100%	+101
4	Wuqi	467770	24.26	120.52	32	100%	100%	+73
5	Alishan	467530	23.51	120.81	2413	90%	100%	+72
<i>Northern</i>								
6	Anbu	466910	25.18	121.53	838	80%	100%	+71
7	Taipei	466920	25.04	121.51	6	70%	100%	+37
8	Keelung	466940	25.13	121.74	27	100%	100%	-18
9	Tamsui	466900	25.16	121.45	19	100%	100%	-159
10	Banqiao	466880	25.00	121.44	10	100%	0%	—
<i>Eastern / southeastern monsoon coast</i>								
11	Chenggong	467610	23.10	121.37	34	100%	100%	+16
12	Hualien	466990	23.98	121.61	16	90%	100%	-33
13	Dawu	467540	22.36	120.90	8	80%	100%	-66
14	Taitung	467660	22.75	121.15	9	70%	100%	-200
15	Yilan	467080	24.76	121.76	7	80%	100%	-227
16	Suao	467060	24.60	121.86	25	40%	100%	-250
17	Hengchun	467590	22.00	120.75	22	80%	100%	-254
<i>Western / southern lowland (SPI-3 mostly silent)</i>								
18	Chiayi	467480	23.50	120.43	27	80%	100%	-281
19	Xinwu	467050	25.01	121.05	21	100%	0%	—
20	Tainan	467410	22.99	120.20	41	60%	0%	—
21	Yongkang	467420	23.04	120.24	8	40%	0%	—
22	Kaohsiung	467440	22.57	120.32	2	60%	0%	—

CRediT authorship contribution statement

Foo Hui-Mean: Data curation, Formal analysis, Investigation, Validation, Resources, Writing – review & editing. **Yuan-chin Ivan Chang:** Conceptualization, Methodology, Software, Formal analysis, Writing – original draft, Writing – review & editing, Supervision.

Declaration of competing interest

The authors declare that they have no known competing financial interests or personal relationships that could have appeared to influence the work reported in this paper.

References

- [1] Chen, C.-S. and Chen, Y.-L. (2003). The rainfall characteristics of Taiwan. *Monthly Weather Review*, **131**(7), 1323–1341. doi: [https://doi.org/10.1175/1520-0493\(2003\)131%3C1323:TRCOT%3E2.0.CO;2](https://doi.org/10.1175/1520-0493(2003)131%3C1323:TRCOT%3E2.0.CO;2).
- [2] Dadson, S. J., Hovius, N., Chen, H., Dade, W. B., Hsieh, M.-L., Willett, S. D., Hu, J.-C., Horng, M.-J., Chen, M.-C., Stark, C. P., Lague, D. and Lin, J.-C. (2003). Links between erosion, runoff variability and seismicity in the Taiwan orogen. *Nature*, **426**(6967), 648–651. doi: <https://doi.org/10.1038/nature02150>.
- [3] Kao, S.-J. and Milliman, J. D. (2008). Water and sediment discharge from small mountainous rivers, Taiwan: The roles of lithology, episodic events, and human activities. *The Journal of Geology*, **116**(5), 431–448. doi: <https://doi.org/10.1086/590921>.
- [4] Vo, T. H. and Liou, Y. A. (2024). Four-decade spring droughts in Taiwan. *Journal of Hydrology: Regional Studies*, **54**, Article 101849. doi: <https://doi.org/10.1016/j.ejrh.2024.101849>.
- [5] Doob, J. L., 1953: *Stochastic Processes*. Wiley, 654 pp.
- [6] Cho, K., B. van Merriënboer, C. Gulcehre, D. Bahdanau, F. Bougares, H. Schwenk, and Y. Bengio, 2014: Learning phrase representations using RNN encoder–decoder for statistical machine translation. *Proc. 2014 Conf. Empirical Methods in Natural Language Processing*, Doha, Qatar, Association for Computational Linguistics, 1724–1734, doi:10.3115/v1/D14-1179.
- [7] Hochreiter, S., and J. Schmidhuber, 1997: Long short-term memory. *Neural Comput.*, **9**, 1735–1780, doi:10.1162/neco.1997.9.8.1735.
- [8] Espeholt, L., and Coauthors, 2022: Deep learning for twelve hour precipitation forecasts. *Nat. Commun.*, **13**, 5145.
- [9] Funk, C., and Coauthors, 2015: The climate hazards infrared precipitation with stations—a new environmental record for monitoring extremes. *Sci. Data*, **2**, 150066.
- [10] Gama, J., I. Žliobaitė, A. Bifet, M. Pechenizkiy, and A. Bouchachia, 2014: A survey on concept drift adaptation. *ACM Comput. Surv.*, **46**(4), Article 44, 37 pp.
- [11] Hao, Z., X. Yuan, Y. Xia, F. Hao, and V. P. Singh, 2017: An overview of drought monitoring and prediction systems at regional and global scales. *Bull. Amer. Meteor. Soc.*, **98**, 1879–1896, doi:10.1175/BAMS-D-15-00149.1.
- [12] Hersbach, H., and Coauthors, 2020: The ERA5 global reanalysis. *Quart. J. Roy. Meteor. Soc.*, **146**, 1999–2049.

- [13] Hundman, K., V. Constantinou, C. Laporte, I. Colwell, and T. Soderstrom, 2018: Detecting spacecraft anomalies using LSTMs and nonparametric dynamic thresholding. *Proc. 24th ACM SIGKDD*, 387–395.
- [14] Milly, P. C. D., J. Betancourt, M. Falkenmark, R. M. Hirsch, Z. W. Kundzewicz, D. P. Lettenmaier, and R. J. Stouffer, 2008: Stationarity is dead: Whither water management? *Science*, **319**, 573–574.
- [15] Roe, G. H., 2005: Orographic precipitation. *Annu. Rev. Earth Planet. Sci.*, **33**, 645–671.
- [16] McKee, T. B., N. J. Doesken, and J. Kleist, 1993: The relationship of drought frequency and duration to time scales. *Proc. 8th Conf. on Applied Climatology*, Anaheim, CA, AMS, 179–184.
- [17] Menne, M. J., I. Durre, R. S. Vose, B. E. Gleason, and T. G. Houston, 2012: An overview of the Global Historical Climatology Network-Daily database. *J. Atmos. Oceanic Technol.*, **29**, 897–910.
- [18] Moustakides, G. V., 1986: Optimal stopping times for detecting changes in distributions. *Ann. Statist.*, **14**, 1379–1387.
- [19] Muñoz-Sabater, J., and Coauthors, 2021: ERA5-Land: A state-of-the-art global reanalysis dataset for land applications. *Earth Syst. Sci. Data*, **13**, 4349–4383.
- [20] Ravuri, S., and Coauthors, 2021: Skilful precipitation nowcasting using deep generative models of radar. *Nature*, **597**, 672–677.
- [21] Shi, X., and Coauthors, 2015: Convolutional LSTM network: A machine learning approach for precipitation nowcasting. *Adv. Neural Inf. Process. Syst.*, 802–810.
- [22] Sloughter, J. M., A. E. Raftery, T. Gneiting, and C. Fraley, 2007: Probabilistic quantitative precipitation forecasting using Bayesian model averaging. *Mon. Wea. Rev.*, **135**, 3209–3220.
- [23] Wang, Y., M. Long, J. Wang, Z. Gao, and P. S. Yu, 2017: PredRNN: Recurrent neural networks for predictive learning using spatiotemporal LSTMs. *Adv. Neural Inf. Process. Syst.*, 879–888.
- [24] World Meteorological Organization, 2012: Standardized Precipitation Index User Guide. WMO-No. 1090, 24 pp.
- [25] Lorenz, E. N., 1969: The predictability of a flow which possesses many scales of motion. *Tellus*, **21**, 289–307.
- [26] Ropelewski, C. F., and M. S. Halpert, 1987: Global and regional scale precipitation patterns associated with the El Niño/Southern Oscillation. *Mon. Wea. Rev.*, **115**, 1606–1626.
- [27] Wang, B., R. Wu, and K.-M. Lau, 2001: Interannual variability of the Asian summer monsoon: contrasts between the Indian and the western North Pacific–East Asian monsoons. *J. Climate*, **14**, 4073–4090.

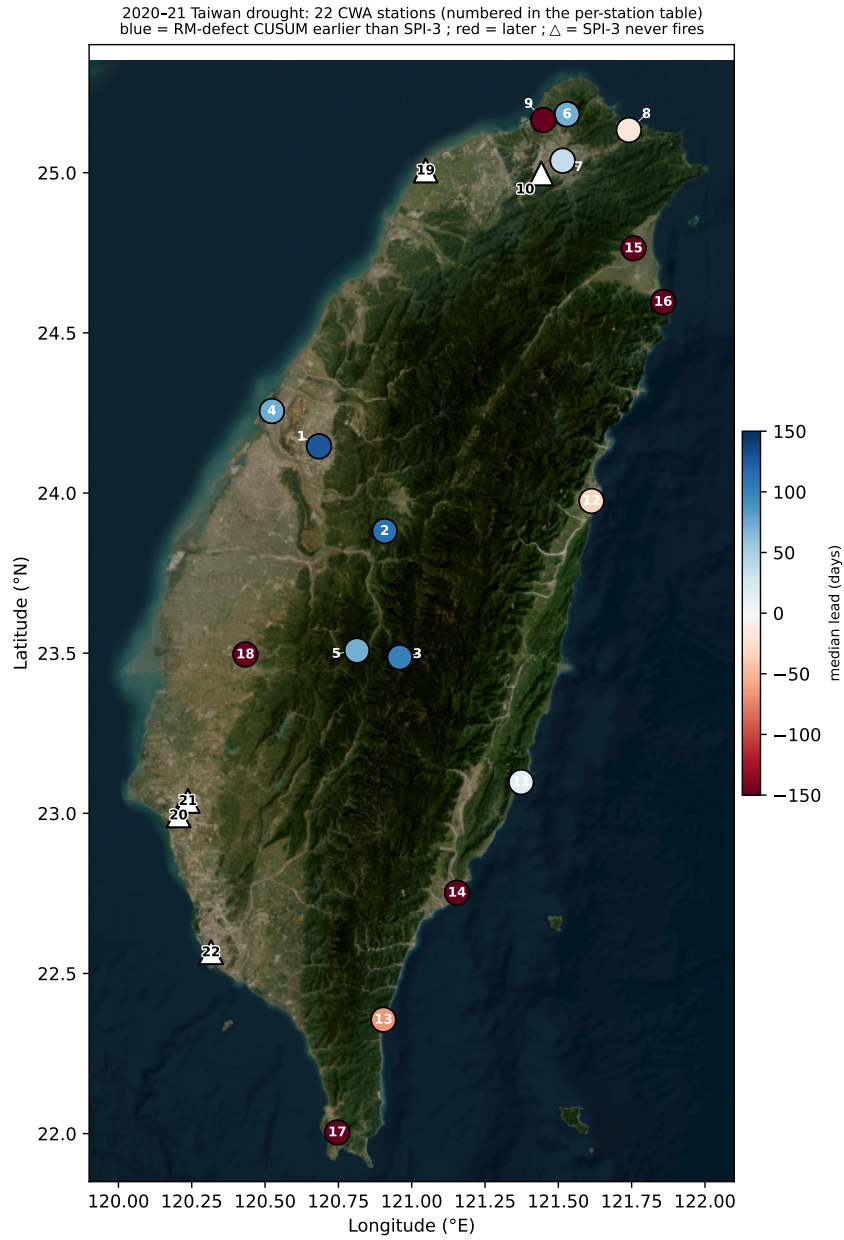


Figure 2: Per-station early-warning lead of the RM-defect CUSUM over the SPI-3 CUSUM on the real 2020–2021 Taiwan drought (seed median over ten seeds, matched ARL_0), mapped to the real CWA station locations. Numbers key each station to Table 11 (which lists names, coordinates, and detection rates). Blue = RM detector earlier, red = SPI-3 earlier; open triangles mark stations where the SPI-3 baseline never fires. The lead is organised by terrain: RM leads by two to four months over the central mountain water-supply catchments (the reservoir headwaters), lags on the wetter eastern and southeastern monsoon coasts, and recovers a signal the accumulation index misses in the southwestern lowlands; the central mountain range visible in the satellite basemap is the orographic control. Station coordinates from the CWA/CODiS station list; satellite imagery courtesy of Esri World Imagery (Esri, Maxar, Earthstar Geographics); generated by `plot_taiwan_drought_map.py`.

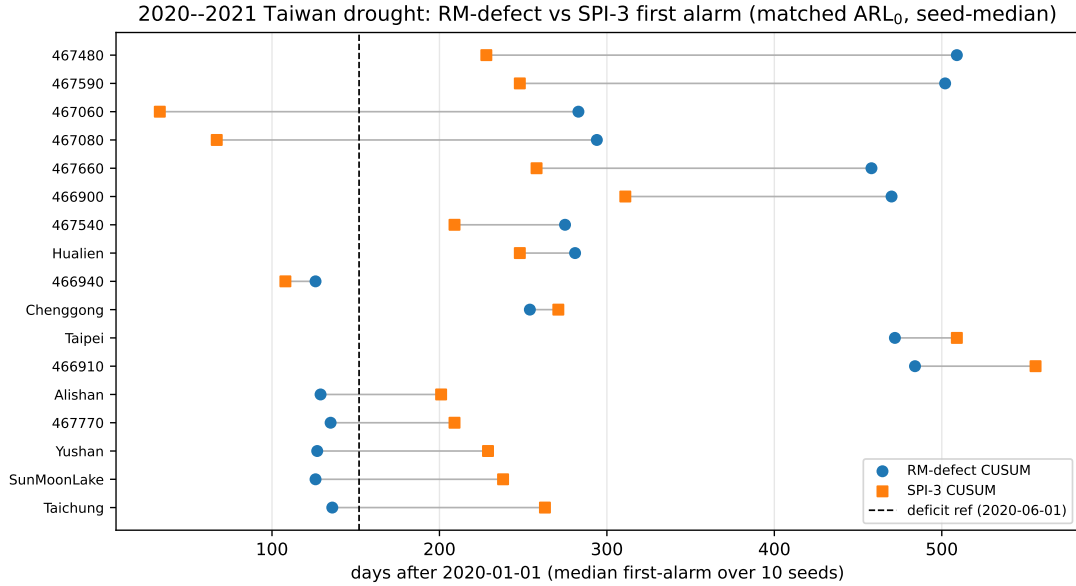


Figure 3: First-alarm day for the RM-defect CUSUM (circles) and the SPI-3 CUSUM (squares) on the real 2020–2021 Taiwan drought, per station (seed median over ten seeds), at matched ARL_0 , for the 22-station island-wide set. Horizontal segments join the two detectors at each station; the dashed line marks the documented June-2020 deficit reference. Stations are ordered by lead. The RM detector (blue) alarms well ahead of the accumulation baseline (orange) over the central water-supply catchments at the top, but lags it on the wetter eastern/southeastern coast at the bottom, so the island-wide median lead is not significant (Table 4). Generated by `run_taiwan_drought_warning.py`.

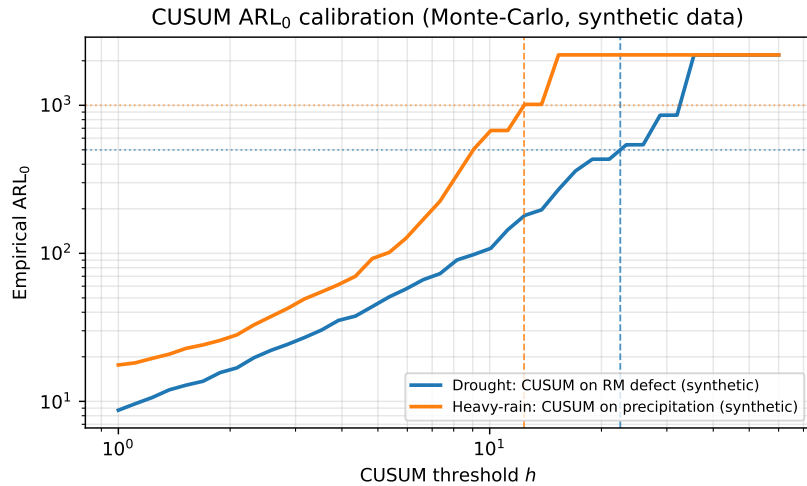


Figure 4: Monte-Carlo CUSUM ARL_0 calibration on the synthetic testbed, two curves on a single panel: the drought detector (CUSUM on the standardized RM defect) and the heavy-rain detector (CUSUM on precipitation). Empirical ARL_0 (reset-on-crossing on a six-year null stream) increases monotonically with the threshold h . Horizontal dotted lines mark the target ARL_0 (500 and 1,000); vertical dashed lines mark the calibrated h^* where each curve meets its target ($h^* \approx 22.5$ drought, $h^* \approx 12.4$ heavy-rain). Curves flatten at large h where the finite null stream yields no crossing.

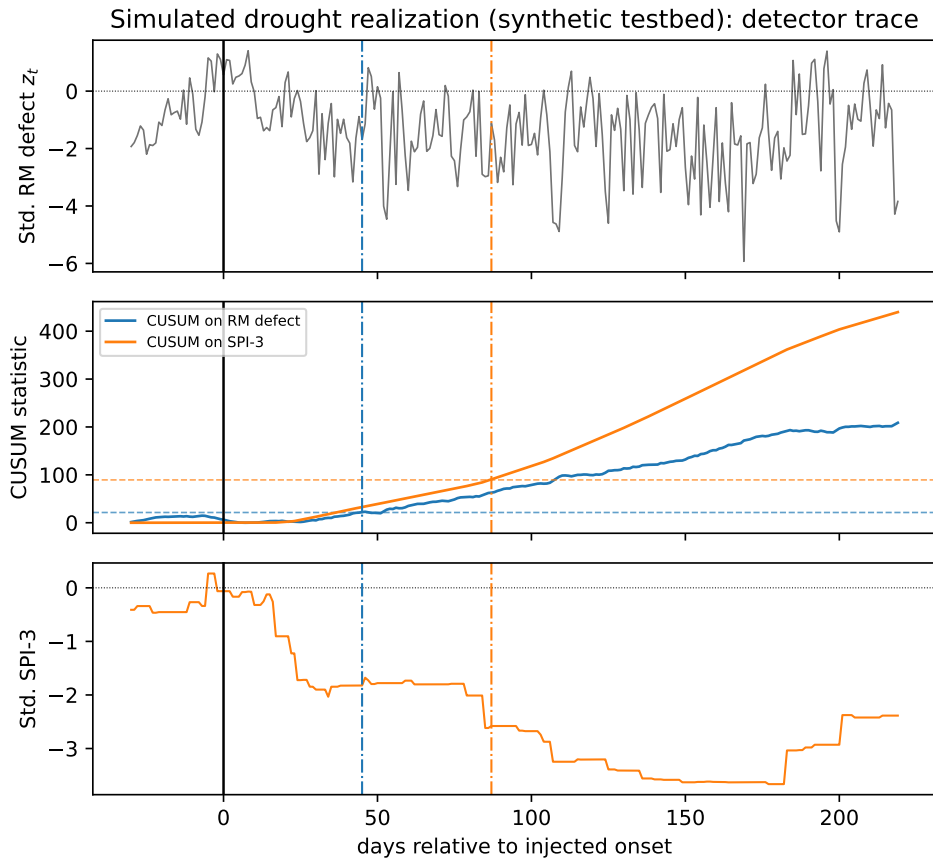


Figure 5: One simulated drought realization (synthetic testbed). Top: standardized RM defect z_t . Middle: CUSUM statistics on the RM defect (blue) and on SPI-3 (orange), with calibrated thresholds (dashed) and alarm times (dash-dot verticals). Bottom: standardized SPI-3. The injected onset is at day 0 (black vertical line). Both detectors are calibrated to $ARL_0 = 500$; the RM-defect alarm (day 45) precedes the SPI-3 alarm (day 87), a 42-day lead in this realization.